University of Rhode Island
DigitalCommons@URI

Open Access Dissertations

2017

Performance Analysis and Morphology of Lithium Ion Battery Anodes Prepared by Colloidal Processing

Yuzi Zhang
University of Rhode Island, yuzi_zhang@uri.edu

Follow this and additional works at: https://digitalcommons.uri.edu/oa_diss

Terms of Use
All rights reserved under copyright.

Recommended Citation
Zhang, Yuzi, "Performance Analysis and Morphology of Lithium Ion Battery Anodes Prepared by Colloidal Processing" (2017). *Open Access Dissertations.* Paper 572.
https://digitalcommons.uri.edu/oa_diss/572

This Dissertation is brought to you by the University of Rhode Island. It has been accepted for inclusion in Open Access Dissertations by an authorized administrator of DigitalCommons@URI. For more information, please contact digitalcommons-group@uri.edu. For permission to reuse copyrighted content, contact the author directly.

PERFORMANCE ANALYSIS AND MORPHOLOGY OF LITHIUM ION BATTERY ANODES PREPARED BY COLLOIDAL PROCESSING

BY

YUZI ZHANG

A DISSERTATION SUBMITTED IN PARTIAL FULFILLMENT OF THE REQUIREMENTS FOR THE DEGREE OF

DOCTOR OF PHILOSOPHY

IN

CHEMICAL ENGINEERING

UNIVERSITY OF RHODE ISLAND

2017

DOCTOR OF PHILOSOPHY IN CHEMICAL ENGINEERING

OF

YUZI ZHANG

APPROVED:

Dissertation Committee:

Major Professor Arijit Bose

Stephen Kennedy

Brett L. Lucht

Nasser H. Zawia
DEAN OF THE GRADUATE SCHOOL

UNIVERSITY OF RHODE ISLAND
2017

ABSTRACT

Lithium ion batteries (LIBs) with high power and energy density are desirable for use in portable electronics and electric vehicles. Silicon (Si) and tin (Sn) are among the most promising candidates for LIB anodes owing to their high theoretical specific capacity. However, both Si and Sn suffer from a dramatic volume change during lithiation/delithiation. Extensive efforts have been made using nanostructures to overcome this issue and improve the electrochemical performance of Si and Sn anodes. Carbon black (CB) is usually added to either electrode in LIBs to provide electrical conductivity. Because CB does not contribute to capacity, minimizing its use can lower the mass of battery to further increase the energy density. Due to the high aspect ratio and excellent electrical conductivity, sheet-like material reduced graphene oxide (RGO) is able to form a conducting network at much lower volume fractions than CB based on the percolation theory.

In this work, Si and Sn based anodes were prepared respectively using an emulsion-templating strategy where active material nanoparticles were confined in the oil phase of the formed emulsions. CB stabilized these emulsions and formed a conductive network. We reduced the total carbon loading of Si anode by replacing a small amount of CB with RGO. In Si anode with a lower total carbon content, the formation of a conducting network consisting of CB and RGO contributed to a good cycle performance, which is comparable to the anode with double carbon loading but no RGO. We also studied the influence of the oil on the structure and electrochemical behavior of emulsion-templated Sn based anode. Density and vapor pressure of the oils affected the creaming and drying rates of the emulsions, which in turn affected the structures of

dried emulsions and anode performance. Emulsion droplet size also had an impact on the drying process. Sn anode prepared with hexadecane that had a smaller density than water and a low vapor pressure along with smaller oil droplet showed the highest capacity and capacity retention which were attributed to the smooth and dense morphology with no cracking. Aqueous suspensions of CB and mixtures of CB and RGO were also examined. It was found that the concentrations of CB and pH conditions played major roles in determining the rheological properties and microstructures of the suspensions. The combinations of optical microscopy, cryogenic and conventional scanning electron microscopy, transmission electron microscopy were used to characterize the structures of fresh emulsions, dried emulsions (anodes) and suspensions throughout this dissertation.

ACKNOWLEDGMENTS

First of all, I would like to express my sincere gratitude to my thesis advisor Dr. Arijit Bose, for his valuable support and guidance throughout my time at URI. He has always motivated me to think independently and conduct research with a clear goal. I'm also grateful to his patience, encouragement and faith in me which have accompanied me to work hard toward my degree.

I would also like to extend my appreciation to my committee members Dr. Brett L. Lucht, Dr. Stephen Kennedy and Dr. David R. Heskett, for their precious time and invaluable inputs on my research. I am grateful to my collaborative lab professor Dr. Brett L. Lucht, for his support and invaluable suggestions on my projects. I also thank Dr. Richard Brown and Dr. Geoffrey D. Bothun for allowing me to use their labs.

I am thankful to my collaborator who is also my friend Yue Pan, for her constant assistance in electrochemical testing and helpful discussions. I would like to thank Dr. Everett E. Crisman and Dr. Richard Kingsley for their training and help on SEM and TEM. I am grateful to Hari Katepalli for helping me with his patience and sharing his knowledge when I was learning and operating cryo-SEM. I thank Joe Sullivan for his timely help and inputs with rheology tests. I also thank my other labmates and fellow graduate students for their help and cooperation in using the labs. I would like to thank our staff members Brenda and Marilu for helping me with paperwork and office issues.

I thank all my friends for their help, support and the wonderful time we had together during my stay at URI. Special thanks go to my friend Yanan Li who generously offered her place for me to stay over the last period of my time at URI.

Last but most importantly, I am very much grateful to my beloved husband Lin Du for always being with me, showing his support and trying his best to assist me in completing my thesis. I am also deeply indebted to my dear parents who always have faith in me, support and love me unconditionally in the past years. It is their continued encouragement that made me go so far toward my life goals.

PREFACE

This dissertation is written in manuscript format. The first chapter is an introduction covering the main topics of the dissertation. The second chapter entitled "Towards Reducing Carbon Content in Silicon/Carbon Anodes for Lithium Ion Batteries" was published in Carbon (*Carbon* 112 (2017): 72-78) in February 2017. The third chapter entitled "The Influence of the Oil on the Structure and Electrochemical Performance of Emulsion-Templated Tin/Carbon Anodes for Lithium Ion Batteries" is in preparation for ACS Applied Materials & Interfaces. The fourth chapter entitled "Microstructures and Rheological Behavior for Aqueous Suspensions of Carbon Black and Mixtures of Carbon Black and Reduced Graphene Oxide" is in preparation for Colloids and Surfaces A: Physicochemical and Engineering Aspects.

TABLE OF CONTENTS

LIST OF TABLES

TABLE PAGE

LIST OF FIGURES

CHAPTER 1

1.1 Introduction

A battery cell is a device that converts its chemical energy that is stored in its two electrodes into electrical energy through internal chemical reactions. If the chemical reactions are reversible and the cell can be recharged for many times, it's called a rechargeable battery or secondary battery. Lithium ion battery (LIB) is one of these batteries which utilizes insertion reactions for both positive and negative electrodes with Li ions as charge carriers.[1]

A typical LIB is composed of an anode (negative), a cathode (positive), an electrolyte and a separator. The positive electrodes are usually Li-containing metal oxides with a layered structure, such as lithium cobalt oxide ($LiCoO_2$), or tunnel-structured materials such as lithium manganese oxide ($LiMn_2O_4$). The negative electrodes comprise insertion-type materials such as carbon and TiO_2, conversion-type materials such as iron oxides and cobalt oxides, and alloying-type materials such as Si and Sn. The electrolyte is Li ion conductive but electronically insulated. It's commonly an organic solvent mixture with dissolved inorganic lithium salt in the solvents. The separator is also necessary in the battery which prevents the short circuit between two electrodes and also allows Li ions to transport during charging/discharging.

The schematic description of a lithium ion cell is shown in Figure 1.1.[2] The ongoing electrochemical process is the deintercalation of Li ions from the graphitic structure of anode and the simultaneous intercalation into the layered structure of cathode. This is a discharge process of the cell; the reversed reaction occurs in the charge process.

Dissociated Li ions are transported between the anode and the cathode through the electrolyte.

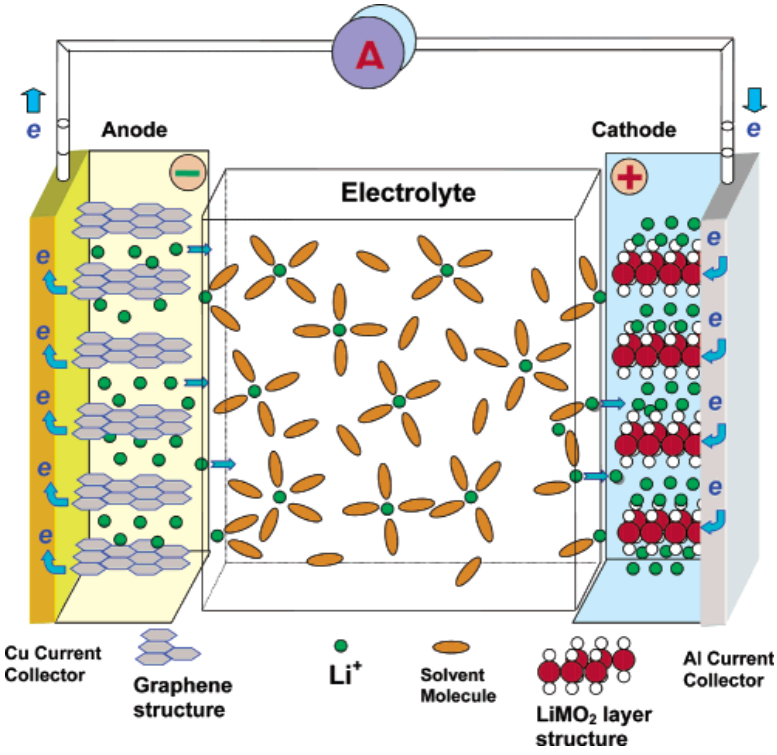

Figure 1.1. Schematic showing a lithium ion cell that employs a graphitic carbon as the anode and a transitional metal oxide as the cathode.[2]

Since the commercialization in the early 1990s, LIBs have become the most important and widely used battery, mostly as the power source for portable electronic devices, such as tablets, laptops and smart phones. The advantages of LIBs are high power density, high energy density, long cycle life, good environmental compatibility, and light weight over conventional lead-acid batteries and Ni-based batteries. Currently, the commercial anode material for LIBs is graphite with a limited theoretical capacity of 372 mAh/g as six carbon atoms can only store one or less Li ion.[3] To improve the low energy and power density of graphite, alternative materials are highly desired.

Silicon (Si) and tin (Sn) are among the most promising materials to replace current carbon anode for LIBs due to their high theoretical capacity (4200 mAh/g for Si and 994 mAh/g for Sn) corresponding to the formation of binary alloys $Li_{22}Si_5$ and $Li_{22}Sn_5$.[4-5] However, the large number of Li ion insertion/extraction into/from Si or Sn causes a large volume change (around 300%), which causes pulverization of the particles and loss of contact with current collector, as well as the formation of a solid electrolyte interphase (SEI) that consumes Li ions as shown in Figure 1.2.[6-7] All these mechanisms contribute to severe capacity fading and poor cycle performance which greatly hinder the applications of Si and Sn anode materials for LIBs.

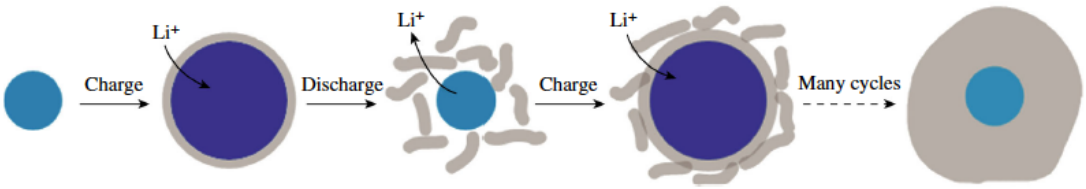

Figure 1.2. Schematic of SEI formation on Si surfaces. A solid Si nanostructure expands during lithiation. A thin SEI layer forms in this lithiated and expanded state. During delithiation process, the Si structures shrink, and the SEI break down into separate pieces, exposing fresh Si surface to the electrolyte. In later cycles, new SEI continues to form on the newly exposed Si surfaces, and this finally results in a very thick SEI layer on the outside of the Si structure.[8]

Extensive efforts have been made to overcome the volume change problem and improve the electrochemical behavior of Si and Sn anodes. Various nanostructures have been designed and developed to accommodate the volume change as nano-sized Si or Sn is less prone to fracture or pulverize.[3, 9] These configurations mainly include nanotubes[8], nanowires[10], core-shell structures[11-12], thin films[13-14], porous structures[15-16] as well as composites with graphene[17-18]. Their electrochemical results show high capacity and good cycle stability.

The techniques reported for preparing Si or Sn anodes usually include complex processing with a long period of fabrication and high cost, such as aerosol spray pyrolysis,[19] forcespinning,[20] freeze-drying and thermal reduction[21]. Emulsification is a process where one liquid is dispersed into another with the assistance of surface-active agents such as amphiphilic surfactants or partially wettable particles. The two liquids to form the emulsions are normally immiscible. Emulsification is a simple colloidal concept and very easy to process. With careful design and implementation, emulsion-templating method can be used for anode preparation which requires drying of the formed emulsions. The properties of two involved liquids in the emulsions such as density and vapor pressure are correlated with the drying procedure.[22-23] Therefore, studying the influence of these properties can help control and improve the cycling performance for the emulsion-templated anodes.

In most LIBs, carbon black (CB) is used in either electrode to improve electrical conductivity between the active particles. With increasing amount of conductive carbon, the electrical electrode resistivity decreases until the critical volume fraction is reached where the electrical resistivity of the electrode sharply drops to a lower level.[24] This critical volume fraction is termed percolation threshold. Since conductive carbon does not contribute to capacity, therefore, to further improve the specific mass capacity of the battery, the amount of CB used in anodes should be reduced without sacrificing the electrical conductivity. Besides the good electrical conductivity, CB shows other advantages such as the properties of reinforcement and coloring, leading to a wide range of commercial applications in tire, ink and plastics.[25-27]

Reduced graphene oxide (RGO) is also an important member in the carbon group besides CB. It is usually obtained through partial chemical or thermal reduction of graphene oxide platelets (GO) by removing the oxygen-containing groups with the recovery of a conjugated structure. Hence the reduced GO (RGO) sheets are usually considered as one class of chemically derived graphene. The graphene structure equips RGO with excellent electrical conductivity, mechanical and optical properties, which give rise to a number of applications in electronics and energy storage.[28-29] Generally, as a sheet-like material, RGO has a large surface area and a high aspect ratio that is in the order of 10^3-10^4. This gives a much lower percolation threshold of RGO compared to that of spherical particles.[30] This feature can be exploited towards reducing carbon content for electrically conductive polymer composites and LIB electrodes where only a small amount of RGO is required to provide good electrical conductivity.

Given the outstanding properties of CB and RGO, investigating their suspensions in terms of rheological behavior and microstructure is important, which can provide insights on how they change with varying conditions such as concentrations and pH. This will promote a better understanding and handling in the manufacturing process. In this study, we utilized emulsion-templating strategy for preparing Si and Sn based anodes with carboxyl-terminated CB as the stabilizer and the conductive agent. In Si based anodes, we replaced a small amount of CB with RGO and reduced the total carbon content of the anode without sacrificing the cycle performance and electrical conductivity. In Sn based anodes, the influence of the oil on the electrochemical performance was investigated and correlated with anode morphology. We also examined the aqueous suspensions of CB as well as the aqueous mixtures of CB and

RGO to study their rheology and microstructure at different concentrations and pH. The combinations of optical microscopy, cryogenic and conventional scanning electron microscopy, transmission electron microscopy were used to characterize the structures of fresh emulsions, dried emulsions (anodes) and suspensions.

1.2 References

1. Shionuma, K.; Yokokawa, M.; Nagaura, T. In *Characteristics of lithium ion rechargeable battery*, Proc. Abstracts 32nd Battery Symp., 1991; pp 33-34.

2. Xu, K., Nonaqueous liquid electrolytes for lithium-based rechargeable batteries. *Chemical reviews* **2004,** *104* (10), 4303-4418.

3. Chen, J., Recent progress in advanced materials for lithium ion batteries. *Materials* **2013,** *6* (1), 156-183.

4. Ma, D.; Cao, Z.; Hu, A., Si-based anode materials for Li-ion batteries: a mini review. *Nano-Micro Letters* **2014,** *6* (4), 347-358.

5. Wang, B.; Luo, B.; Li, X.; Zhi, L., The dimensionality of Sn anodes in Li-ion batteries. *Materials today* **2012,** *15* (12), 544-552.

6. Xiao, X.; Wang, J. S.; Liu, P.; Sachdev, A. K.; Verbrugge, M. W.; Haddad, D.; Balogh, M. P., Phase-separated silicon–tin nanocomposites for high capacity negative electrodes in lithium ion batteries. *Journal of Power Sources* **2012,** *214*, 258-265.

7. Liang, B.; Liu, Y.; Xu, Y., Silicon-based materials as high capacity anodes for next generation lithium ion batteries. *Journal of Power sources* **2014,** *267*, 469-490.

8. Wu, H.; Chan, G.; Choi, J. W.; Yao, Y.; McDowell, M. T.; Lee, S. W.; Jackson, A.; Yang, Y.; Hu, L.; Cui, Y., Stable cycling of double-walled silicon

nanotube battery anodes through solid-electrolyte interphase control. *Nature nanotechnology* **2012,** *7* (5), 310-315.

9. Wu, H.; Cui, Y., Designing nanostructured Si anodes for high energy lithium ion batteries. *Nano Today* **2012,** *7* (5), 414-429.

10. Ge, M.; Rong, J.; Fang, X.; Zhou, C., Porous doped silicon nanowires for lithium ion battery anode with long cycle life. *Nano letters* **2012,** *12* (5), 2318-2323.

11. Chen, S.; Gordin, M. L.; Yi, R.; Howlett, G.; Sohn, H.; Wang, D., Silicon core–hollow carbon shell nanocomposites with tunable buffer voids for high capacity anodes of lithium-ion batteries. *Physical Chemistry Chemical Physics* **2012,** *14* (37), 12741-12745.

12. Jung, Y. S.; Lee, K. T.; Ryu, J. H.; Im, D.; Oh, S. M., Sn-carbon core-shell powder for anode in lithium secondary batteries. *Journal of the Electrochemical Society* **2005,** *152* (7), A1452-A1457.

13. Lee, K.-L.; Jung, J.-Y.; Lee, S.-W.; Moon, H.-S.; Park, J.-W., Electrochemical characteristics of a-Si thin film anode for Li-ion rechargeable batteries. *Journal of Power Sources* **2004,** *129* (2), 270-274.

14. Li, J.; Yang, F.; Ye, J.; Cheng, Y.-T., Whisker formation on a thin film tin lithium-ion battery anode. *Journal of Power Sources* **2011,** *196* (3), 1474-1477.

15. Kim, H.; Han, B.; Choo, J.; Cho, J., Three‐dimensional porous silicon particles for use in high‐performance lithium secondary batteries. *Angewandte Chemie* **2008,** *120* (52), 10305-10308.

16. Xu, Y.; Guo, J.; Wang, C., Sponge-like porous carbon/tin composite anode materials for lithium ion batteries. *Journal of Materials Chemistry* **2012,** *22* (19), 9562-9567.

17. Xiang, H.; Zhang, K.; Ji, G.; Lee, J. Y.; Zou, C.; Chen, X.; Wu, J., Graphene/nanosized silicon composites for lithium battery anodes with improved cycling stability. *Carbon* **2011,** *49* (5), 1787-1796.

18. Wang, G.; Wang, B.; Wang, X.; Park, J.; Dou, S.; Ahn, H.; Kim, K., Sn/graphene nanocomposite with 3D architecture for enhanced reversible lithium storage in lithium ion batteries. *Journal of Materials Chemistry* **2009,** *19* (44), 8378-8384.

19. Xu, Y.; Liu, Q.; Zhu, Y.; Liu, Y.; Langrock, A.; Zachariah, M. R.; Wang, C., Uniform nano-Sn/C composite anodes for lithium ion batteries. *Nano letters* **2013,** *13* (2), 470-474.

20. Agubra, V. A.; Zuniga, L.; De la Garza, D.; Gallegos, L.; Pokhrel, M.; Alcoutlabi, M., Forcespinning: A new method for the mass production of Sn/C composite nanofiber anodes for lithium ion batteries. *Solid State Ionics* **2016,** *286*, 72-82.

21. Zhou, X.; Yin, Y.-X.; Wan, L.-J.; Guo, Y.-G., Facile synthesis of silicon nanoparticles inserted into graphene sheets as improved anode materials for lithium-ion batteries. *Chemical communications* **2012,** *48* (16), 2198-2200.

22. Mackay, D.; van Wesenbeeck, I., Correlation of chemical evaporation rate with vapor pressure. *Environmental science & technology* **2014,** *48* (17), 10259-10263.

23. van Wesenbeeck, I.; Driver, J.; Ross, J., Relationship between the evaporation rate and vapor pressure of moderately and highly volatile chemicals. *Bulletin of environmental contamination and toxicology* **2008,** *80* (4), 315-318.

24. Spahr, M. E.; Goers, D.; Leone, A.; Stallone, S.; Grivei, E., Development of carbon conductive additives for advanced lithium ion batteries. *Journal of Power Sources* **2011,** *196* (7), 3404-3413.

25. Sumita, M.; Sakata, K.; Asai, S.; Miyasaka, K.; Nakagawa, H., Dispersion of fillers and the electrical conductivity of polymer blends filled with carbon black. *Polymer Bulletin* **1991,** *25* (2), 265-271.

26. Medalia, A., Effect of carbon black on dynamic properties of rubber vulcanizates. *Rubber chemistry and Technology* **1978,** *51* (3), 437-523.

27. Mansour, K.; Soileau, M.; Van Stryland, E. W., Nonlinear optical properties of carbon-black suspensions (ink). *JOSA B* **1992,** *9* (7), 1100-1109.

28. Eda, G.; Fanchini, G.; Chhowalla, M., Large-area ultrathin films of reduced graphene oxide as a transparent and flexible electronic material. *Nature nanotechnology* **2008,** *3* (5), 270-274.

29. Zhu, X.; Zhu, Y.; Murali, S.; Stoller, M. D.; Ruoff, R. S., Nanostructured reduced graphene oxide/Fe2O3 composite as a high-performance anode material for lithium ion batteries. *Acs Nano* **2011,** *5* (4), 3333-3338.

30. Zhang, Y.; Pan, Y.; Chen, Y.; Lucht, B. L.; Bose, A., Towards reducing carbon content in silicon/carbon anodes for lithium ion batteries. *Carbon* **2017,** *112*, 72-78.

CHAPTER 2

Towards Reducing Carbon Content in Silicon/Carbon Anodes for Lithium Ion Batteries

Published in *Carbon*, **2017**, 112, 72-78

Yuzi Zhang[1], Yue Pan[2], Yanjing Chen[1], Brett L. Lucht[2], Arijit Bose[1,*]

[1] Department of Chemical Engineering,

[2] Department of Chemistry, University of Rhode Island, Kingston, Rhode Island, 02881

* Corresponding author: bosea@uri.edu, 401-874-2804

2.1 Abstract

Conducting carbon is added to electrodes of lithium ion batteries (LIBs) to provide electrical conductivity. Because this carbon does not contribute to capacity, there is a significant drive towards decreasing its content with a goal of lowering the mass of the electrode. Reduced graphene oxide (RGO) has a high electrical conductivity, and is a potential alternative to traditionally used conductive carbon black (CB) in anodes for LIBs. Importantly, because of its high aspect ratio, RGO is expected to form a conducting network at much lower volume loadings than CB. We report the use of this concept to significantly reduce carbon loading in silicon-carbon (Si-C) anodes for LIBs that are formed by emulsion-templating. An anode with 1 wt% RGO and 14 wt% CB (15 wt% total carbon) showed specific capacity and capacity retention that was comparable to an anode with 30 wt% CB with or without RGO. The capacity retention was significantly lower for the anode with 15 wt% total carbon that had no RGO. Cryo-SEM imaging of the emulsions, SEM imaging of the dried emulsion, and electrochemical impedance spectroscopy confirmed the formation of a conducting carbon network at 15 wt% total carbon loading when 1 wt% of the CB was replaced with RGO, and the lack of a well-connected network without the RGO. While this concept has been demonstrated for anodes for LIBs, the framework is relevant for other applications where electrical conductivity at minimum carbon content is desired.

2.2 Introduction

Lithium ion batteries (LIBs) with high energy density are desirable for use in advanced electronic devices and electric vehicles.[1-6] Because high electron conductivity is required for the anode and cathode, conductive carbon black (CB) is

usually added to either electrode. The conductive carbon additive does not contribute to electrode capacity, and one important goal in LIBs electrode design is to minimize its use, thus increasing the specific mass capacity of the battery.[7-10]

The volume fraction loading at the percolation threshold indicates the minimum amount of conducting filler needed to impart conductivity to an insulating matrix.[11-12] For monodispersed solid spheres, the percolation threshold $ø_{sphere} = 0.29$.[13] When fractal particles, such as CB are deployed, their effective volume fraction in a suspension can be estimated using the following equation,[14-15]

$$\frac{ø_{eff}}{ø_o} = (D/D_0)^{3-f} \quad , \qquad (1)$$

where $ø_{eff}$ and $ø_o$ are the effective and actual volume fractions of the CB particles in the suspension, D is the hydrodynamic diameter of the fractal CB particle (~120 nm), D_0 is diameter of the primary particle in the CB (~20 nm) and f is the mass fractal dimension of the particle. $D/D_0 = 6$, and the fractal dimension f for the CB particles is 2.2.[16] Eq. (1) shows that the effective volume fraction occupied by these CB particles would be ~4 times the volume fraction occupied by the same mass of spherical particles. This lower material requirement is one of the key reasons behind the use of fractal CB rather than dense spherical carbon particles to enhance electrode conductivity. For sheet-like materials, the percolation threshold $ø_{sheet} \sim ø_{sphere}/AR$,.[13, 17] The aspect ratio $AR = L/t$, where L is the lateral dimension, and t is the sheet thickness. AR for reduced graphene oxide (RGO) is typically of the order of $10^3 – 10^4$. Given the much lower percolation threshold for sheet-like materials of high aspect ratio and the high electrical conductivity of RGO, we hypothesized that replacing some of the CB

with RGO would reduce the total carbon used in an electrode without sacrificing electrical conductivity. We examined the hypothesis in this work.

In previous work, we used emulsion-templating for forming silicon-based anodes that showed good electrochemical performance.[18] CB particles were used to stabilize emulsions as well as form a conducting carbon network. The organization of silicon nanoparticles (SiNPs) into porous carbon cages formed by the CB allowed expansion and contraction of the SiNPs during lithiation and delithiation without pulverization and without disrupting the conducting carbon network. In this paper, we show that when a small fraction of the conducting carbon comes from RGO, the total carbon content of an anode prepared by emulsion-templating can be lowered significantly without sacrificing electrochemical performance.

2.3 Experiments

2.3.1 Preparation of anodes

SiNPs (average diameter ~50 nm) were purchased from Alfa Aesar. A para-amino benzoic acid-terminated CB (specific surface area of CB ~200 m^2/g) suspension in water at pH 7.5 was obtained from Cabot Corporation. While the surface treatment for this CB introduces electrical resistance, the surface functionality is important for stabilizing emulsions. At neutral pH, the carboxyl groups on the CB particles are deprotonated. These CB particles are highly hydrophilic and form a stable suspension in water. Reduced graphene oxide particles (RGO) were obtained from Graphene Supermarket. The RGO particles have a specific surface area of ~833 m^2/g and a carbon/oxygen ratio of 10.5. The average lateral dimension of the RGO particles is 4 μm.

The SiNP/CB/RGO anodes were prepared by an emulsion-templating method shown in Figure 2.1. 1M HCl was added to a mixed CB and RGO suspension, or only a CB-containing suspension, until the pH reached 3.3. The addition of the acid protonated some of the surface carboxylate groups on the CB, and made the particles partially hydrophobic. These CB particles favor oil-water interfaces, and stabilize oil-in-water emulsions.[19] In addition, the partially hydrophobic CB particles formed a network in the aqueous phase.[19] When RGO was also present in the suspension, the network contained both entities.

A 2.5 wt% suspension of SiNP in octane was sonicated for 1 hour, and then mixed with the acid-mediated CB and RGO suspension by vortexing for 3 min at 3000 rpm. The volume ratio of the SiNP/octane suspension to the CB/RGO/water suspension was 2:5. An 'octane-in-water' emulsion was formed after vortexing. A 20 mg/ml aqueous binder solution containing polyacrylic acid (PAA) and carboxymethyl cellulose (CMC) in a 1:1 mass ratio was added to the emulsion and vortexed for 5 min.[20-21] The volume of the PAA/CMC solution was adjusted so that the final concentration of binder was 10% of the dried anode mass consisting of SiNP, CB, RGO and binder. The emulsion was transferred on to a CR2032 stainless steel coin cell and dried overnight at 50 ºC under a vacuum, thus removing all the octane and water. The areal loading on the coin cell was ~0.54 mg/cm^2 and the final dried thickness was ~100-150 μm. We examined samples at 30 wt% and 15 wt% total carbon, measured for the dry state. Two classes of samples were prepared at each total carbon loading, one with 1

wt% RGO and the other without RGO. Because the binder concentration was fixed at 10 wt%, reducing the total carbon content meant that the SiNP wt% was increased.

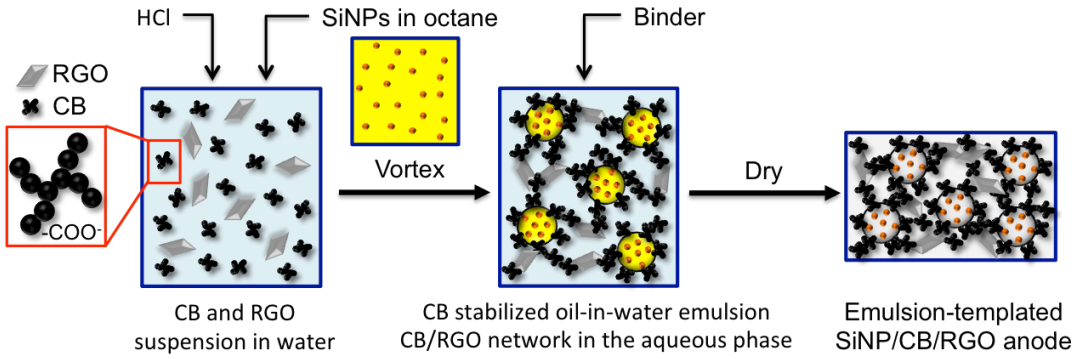

Figure 2.1. Method for preparing the emulsion-templated SiNP/CB/RGO anode. A carboxyl-terminated CB/RGO suspension was formed in water at neutral pH. 1M HCl was added to this suspension, until the pH dropped to 3.3. SiNPs suspended in octane were then added to the CB/RGO suspension and the mixture was vortexed to form octane-in-water emulsions. After a binder solution was added, the emulsion was placed on a coin cell and dried. The SiNP/CB anode (no RGO) was prepared in the same way.

2.3.2 Electrochemical characterization

CR2032 coin cells were assembled in an argon-filled glovebox that had a water vapor concentration of less than 1 ppm. The SiNP-based anodes served as the working electrodes. Lithium foil was employed as the counter electrode. The electrolyte, supplied by BASF, was a mixture of 1.0 M $LiPF_6$ in ethylene carbonate (EC) / diethyl carbonate (DEC) / fluoroethylene carbonate (FEC) at a volumetric ratio of 45:45:10. A polypropylene microporous membrane, Celgard 2325, along with a glass fiber membrane, was used as the separator. Galvanostatic charge/discharge tests were performed on a BST8-WA battery cycler (5 V/1 mA) over the potential range 0.005-1.5 V vs. Li^+/Li, at room temperature, with a cycle rate of 0.1C for 3 cycles followed by 0.2C for 47 cycles, for a total of 50 cycles. The current density, CD, required for each charge or discharge rate was calculated using the following equation:

CD = (Areal loading) (wt% SiNP) (Si theoretical capacity)/ (cycle time). (2)

As an example, for a 60 wt% SiNP sample, Eq. (2) implies a current density of 69 $\mu A/cm^2$ for charge/discharge rates of 0.1C.

Electrochemical Impedance Spectroscopy (EIS) was carried out on a Princeton Instruments V3 Potentiostat, at room temperature. The impedance of each half cell was measured at the 3rd cycle, both in the lithiated state, where the cell potential was 0.15 V, and in the delithiated state where the cell potential was 1.13 V. In addition, EIS spectra were obtained after 50 cycles for the delithiated state, where the cell potential was 1.15 V. The amplitude of the sinusoidal voltage perturbation for EIS was 10 mV and the frequency range was 20 mHz-100 KHz.

2.3.3 Cryogenic scanning electron microscopy (Cryo-SEM)

The microstructures present in the SiNP/CB/RGO and SiNP/CB emulsions were imaged by cryo-SEM using a Gatan Alto 2500 cryo preparation system attached to a Zeiss Sigma VP field emission scanning electron microscope. A small drop containing the emulsion was placed on the sample holder. The sample was frozen rapidly by plunging into liquid nitrogen, then transferred into the preparation chamber maintained at -130 ºC. A flat-edge cold knife in the chamber was utilized to fracture the frozen sample. The chamber was then warmed to -100 ºC for 2 minutes to enhance the surface topology of the sample by differential sublimation. After cooling the chamber back to -130 ºC, the sample was sputter coated with platinum for 60 s, then transferred onto a liquid nitrogen cooled cold stage for imaging at 2 kV.

2.3.4 Scanning electron microscopy (SEM)

Secondary electron imaging on the Zeiss Sigma VP field emission scanning electron microscope was used at 10kV to visualize the dried emulsion samples.

2.4 Results and discussion

We confirmed that the emulsions we prepared were all of the oil-in-water type by adding drops of water or octane to the emulsion.[22] The water drop blended in readily, but the octane drop did not.

The electrochemical performance of the SiNP/CB/RGO and SiNP/CB containing anodes are shown in Figure 2.2. They represent an average from 3 different cells, and the spread in the data are shown as error bars. The specific capacities at the delithiated states of SiNP/CB/RGO and SiNP/CB anodes for 30 wt% and 15 wt% total carbon are shown in Figure 2A. All specific capacity and wt% values were calculated based on the total mass of SiNP, CB, RGO and binder. At 30 wt% total carbon, after 50 cycles, the delithiation capacities were 1287 mAh/g and 1244 mAh/g for the SiNP/CB/RGO and SiNP/CB anodes respectively. At this carbon loading, there was little difference between the performance of anodes with and without RGO. However, for 15 wt% total carbon, the performance of the anode with RGO was significantly better than the one without – the delithiation capacities at 50 cycles were 1370 mAh/g for the SiNP/CB/RGO and 1044 mAh/g for the SiNP/CB anode.

We allowed for initial SEI formation by using charge/discharge rates of 0.1C for the first 3 cycles. The capacity retentions of all the anodes from the 4^{th} cycle onwards, where we used charge/discharge rates of 0.2C, normalized by their respective capacities at the end of the 4^{th} cycle, are shown in Figure 2.2B. The anodes with 30 wt% carbon with and without RGO had capacity retentions of 83% and 80%,

respectively. At this total carbon loading, the replacement of some of the CB with RGO did not provide any advantage. At 15 wt% total carbon with 1 wt% RGO, the capacity retention after 50 cycles was 77%, comparable to the retention for the 30 wt% carbon loading. However, with no RGO, the 15 wt% carbon anode showed a capacity retention of only 61% after 50 cycles. Thus, the total carbon loading can be reduced by a factor of 2, from 30 wt% to 15 wt%, without paying a capacity stability penalty, if only a small amount of RGO is used in combination with CB.

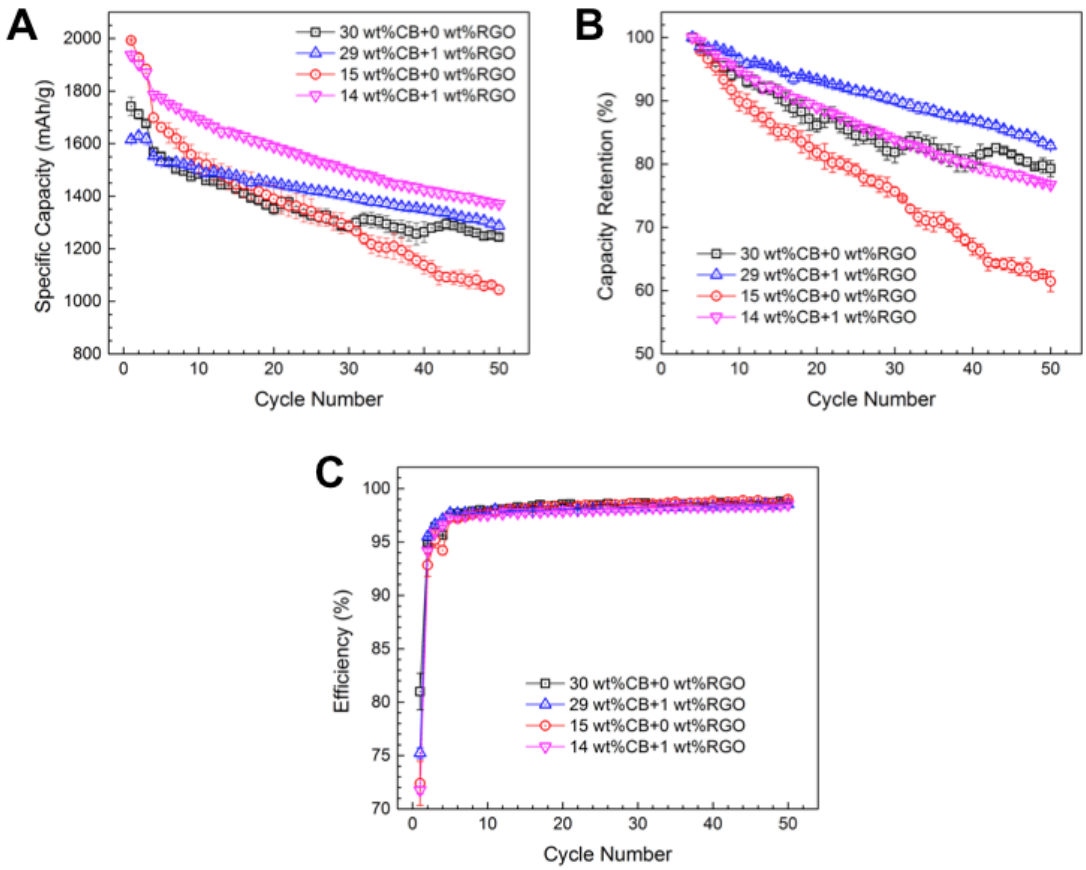

Figure 2.2. Electrochemical characterization of the emulsion-templated Si-based anodes. (A) Delithiation capacity, (B) Delithiation capacity retention (normalized by their respective capacities at the 4th cycle), (C) Coulombic efficiency of SiNP/CB/RGO and SiNP/CB anodes at 30 wt% and 15 wt% total carbon, at a charge/discharge rate of 0.1C for the first 3 cycles followed by 0.2C for 47cycles. The data represent average values from 3 runs. The error bars indicate the maximum spread in the data.

Figure 2.2C shows the Coulombic efficiency for all the anodes. The low efficiency for the first 3 cycles is associated with SEI formation.[23] In the following cycles, the efficiencies varied between 94.5% and 98.9%, indicating that changing the carbon content in our anodes did not lead to modification of lithium ion transport in the cell during charge/discharge cycles.

To further understand the performance of the anodes, electrochemical impedance spectroscopy measurements on SiNP/CB/RGO and SiNP/CB anodes were conducted on samples at delithiated and lithiated states for the 3rd cycle, as well as the delithiated state after 50 cycles. The data for the 3rd cycle provided a window on the state of the anode right after the initial SEI formation. EIS data for the 50th cycle were associated with irreversible changes that occurred to the anode during cycling that affect electrochemical performance.

Nyquist plots, shown in Figures 2.3A, 2.3B and 2.3C, revealed a few important results. All EIS spectra showed a characteristic semicircle corresponding to the charge transfer process, and a linear Warburg component at low frequencies attributed to the diffusion of lithium ions in the anodes. The solution resistance for all the anodes was around 5 ohms cm^2. For 3 cycles, the charge transfer resistance at the lithiated state was lower than that in the delithiated state. After 50 cycles, the charge transfer resistance increased significantly. The charge transfer resistances for the anodes with 30 wt% carbon with and without RGO were comparable, consistent with the capacity data that showed no benefit to replacing some of the CB with RGO at this carbon loading. However, for 15 wt% carbon, the charge transfer resistance for the anode with 1 wt% RGO was significantly lower than the one without RGO, and was

comparable to the resistance from the anodes with 30 wt% carbon. The lower charge transfer resistance is indicative of a better electron-conducting pathway for the SiNP/CB/RGO than the SiNP/CB anode at this total carbon content. The Warburg impedance in the low frequency regions deviated from the ideal case, which should have a slope of 1 in the Nyquist plot. We believe this is a consequence of the roughness of our anodes which varied from sample to sample.[24]

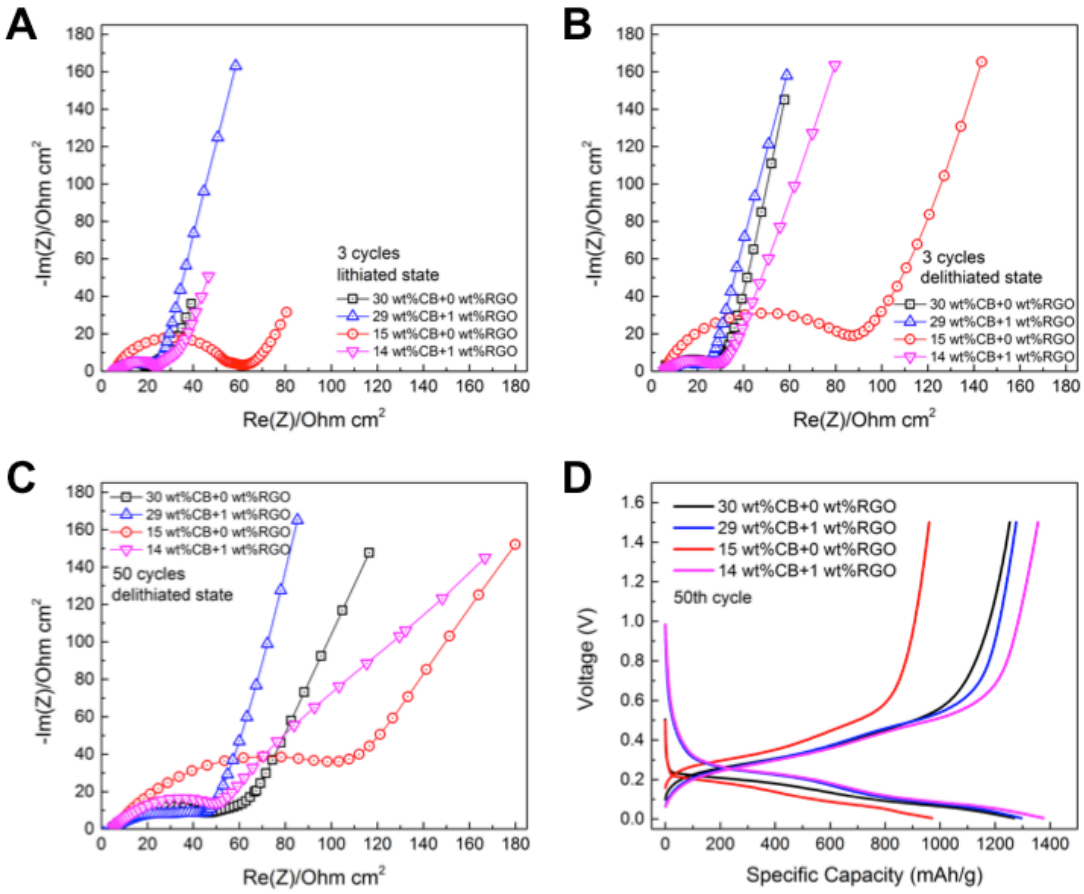

Figure 2.3. Electrochemical impedance spectra of SiNP/CB/RGO and SiNP/CB anodes (A) At a lithiated state for cycle 3. The open circuit potential was 0.15V. (B) At a delithiated state for cycle 3. The open circuit potential was 1.13V. (C) At a delithiated state for cycle 50. The open circuit potential was 1.15V. (D) Voltage profile at the 50th cycle for all the anodes during lithiation and delithiation. The thickness of the lines corresponds to the spread in the data from 3 samples. The voltage gap in the 'plateau region' was the largest for the 15 wt% carbon case with no RGO (red lines).

Figure 2.3D shows the voltage profile at the 50th cycle for all the samples. The 15 wt% carbon anode with 1 wt% RGO showed similar charge and discharge profiles to the anodes with 30 wt% carbon. The 15 wt% carbon anode without RGO showed a voltage gap between the charge and discharge curves in the plateau region that was larger than those for any of the other anodes. The larger voltage gap indicates greater polarization during the charge/discharge process, in agreement with the larger charge transfer resistance measured by EIS.

To further understand the reasons for the variation in electrochemical behavior between the anodes, we sampled the SiNP/CB/RGO and SiNP/CB emulsions using cryo-SEM. Figures 2.4A and 2.4B show octane droplets in water in a SiNP/CB/RGO emulsion, stabilized by CB particles, with the SiNPs confined in the oil phase. For the higher carbon content (30 wt% in dried state), samples with RGO showed a connected carbon network in the aqueous phase (Figures 2.4C, 2.4D). The sample without RGO displayed a partially connected network (Figures 2.4E, 2.4F). For the emulsion with lower carbon loading (15 wt% carbon in dried state, with 1 wt% RGO), a network was formed in the aqueous phase, consisting of RGO particles and CB (Figures 2.4G, 2.4H). However, for samples with lower carbon loading and no RGO (Figures 2.4I, 2.4J), no network was formed. Instead, only some CB aggregates were seen in the aqueous phase.

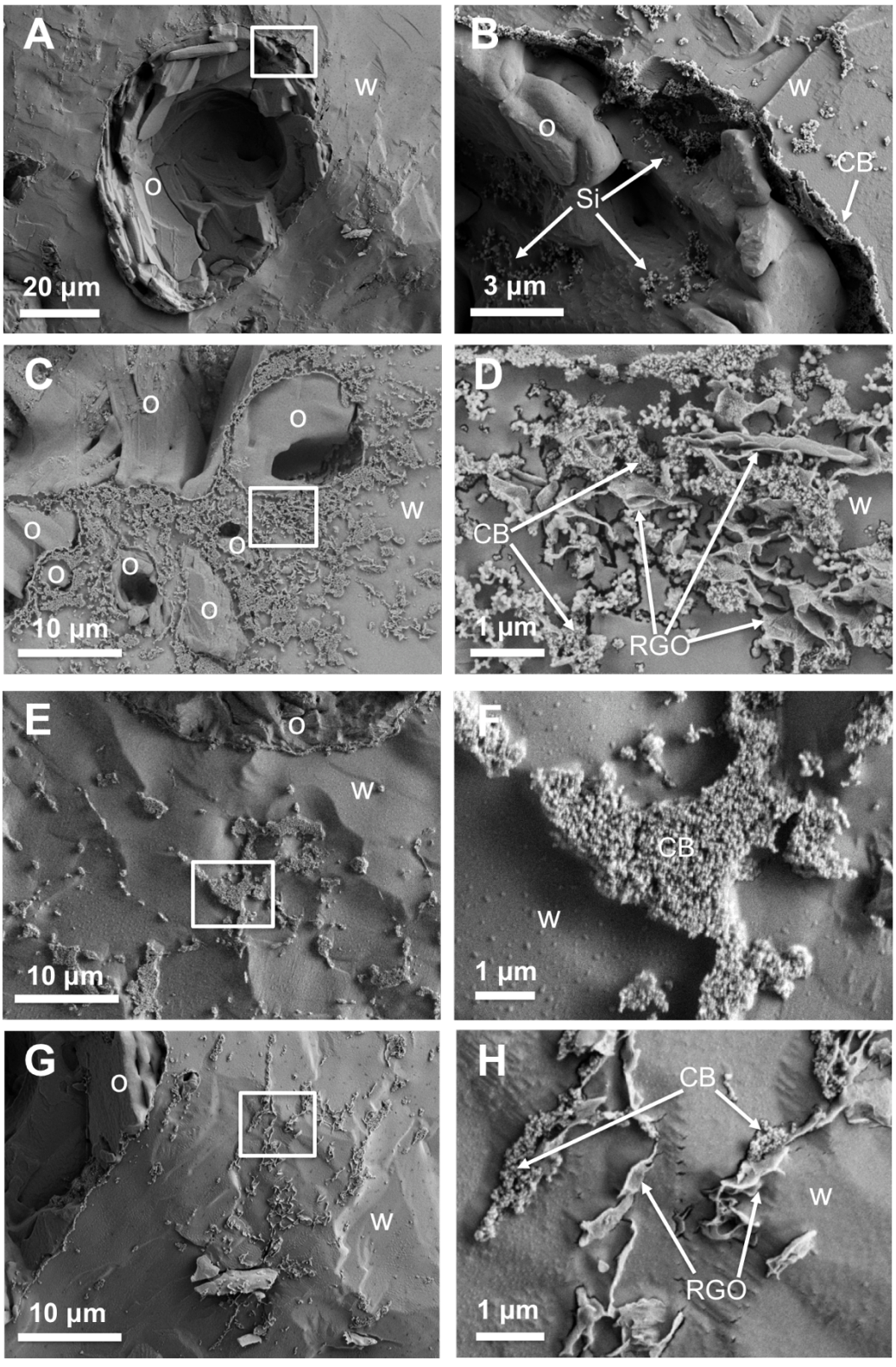
A
W
O
20 µm
B
W
O
CB
Si
3 µm
C
O
O
W
O
O
O
O
O
10 µm
D
W
CB
RGO
1 µm
E
O
W
10 µm
F
CB
W
1 µm
G
O
W
10 µm
H
CB
W
RGO
1 µm

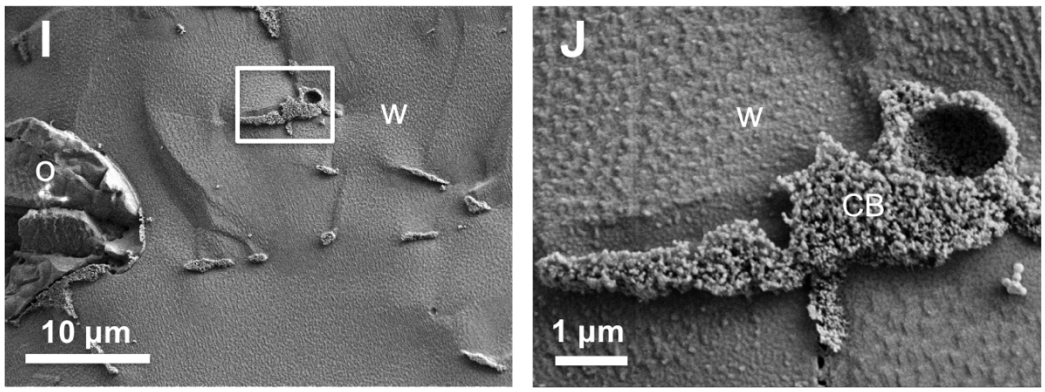

Figure 2.4. Cryo-SEM images of SiNP/CB/RGO (A, B, C, D, G, H) and SiNP/CB (E, F, I, J) emulsions. Magnified images of the regions marked by the white boxes are paired with each image on the left. (A, B) Emulsion with lower total carbon loading (15 wt% in the dried state with14 wt% CB and 1 wt% RGO). An octane-in-water droplet in the SiNP/CB/RGO emulsion, stabilized by CB at the oil-water interface. The SiNPs are confined to the oil phase. (C, D) Emulsion with higher total carbon loading (30 wt% in the dried state, with 29 wt% CB and 1 wt% RGO). The oil droplets are connected by a CB/RGO network in the aqueous phase. (E, F) Emulsion with higher total carbon loading (30 wt% in the dried state, with CB only). The oil droplets are surrounded by a partially connected CB network in the aqueous phase. (G, H) Emulsion with the lower total carbon loading (15 wt% in the dried state, with 14 wt% CB and 1 wt% RGO). RGO particles and the CB form a network. (I, J) Emulsion with lower total carbon loading (15 wt% in the dried state with CB only). No network is formed.

We imaged the dried emulsion samples using SEM. Figures 2.5A, 2.5B and 2.5C show a connected network formed samples with 30 wt % carbon with and without RGO, and 15 wt% carbon with RGO. The lack of a connected carbon network in the 15 wt% carbon sample without RGO, shown in Figure 2.5D, leads to poor electronic conductivity and more extensive capacity fading. This structural information is consistent with the observed capacity behavior and the data from EIS spectra.

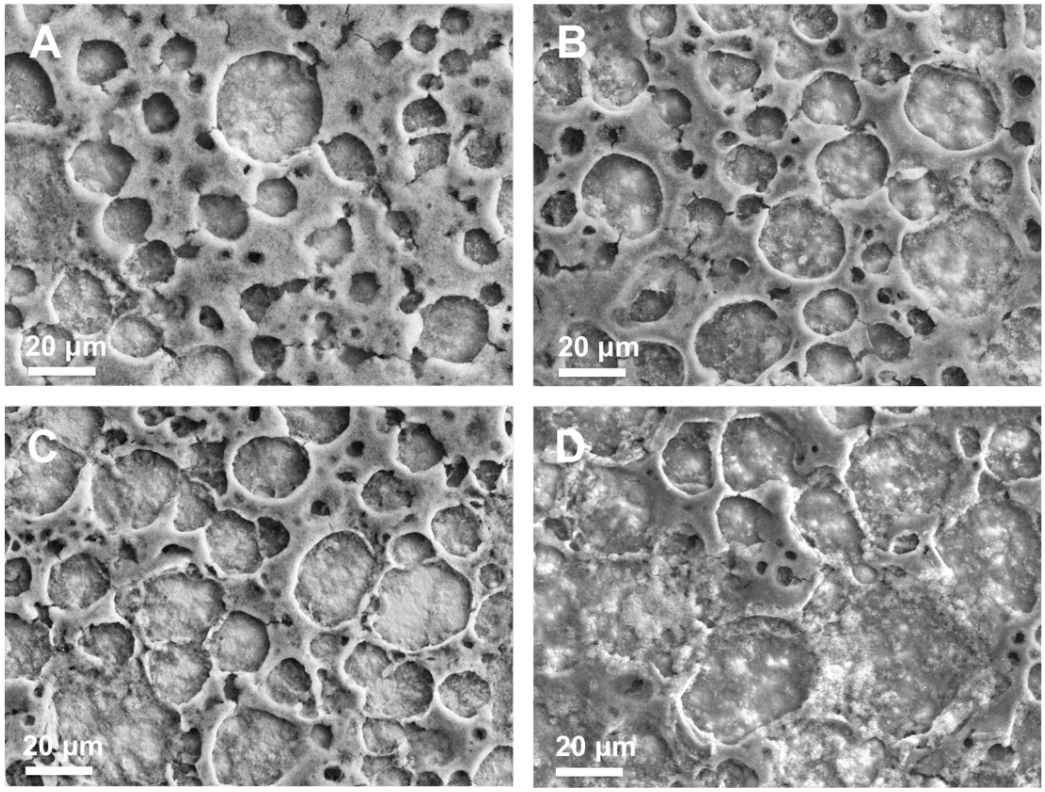

Figure 2.5. SEM images of the dried emulsions with 30 wt% total carbon (A, B) and 15 wt% total carbon (C, D). (A) Sample contains 1 wt% RGO. (B) Sample has no RGO. (C) Sample contains 1 wt% RGO. A connected carbon network is seen in A, B and C. (D) Sample has no RGO. The carbon network is broken in parts, and is only partially connected.

2.5 Conclusions

We demonstrate an effective and simple way to reduce the total carbon content from 30 wt% to 15 wt% in SiNP-based anodes prepared by emulsion-templating. We introduced 1 wt% RGO to the electron-conducting phase along with conductive CB during anode fabrication. For 30 wt% total carbon loading, the replacement of some of the CB with RGO did not impact the electrochemical performance of the anode. The anode with 15 wt% total carbon but with 1 wt% RGO showed electrochemical performance that was comparable to an anode with twice that total carbon loading. Its capacity retention after 50 cycles was much higher than the anode without RGO. The

performance difference for the anodes with 15 wt% total carbon is a consequence of the formation of a carbon network in the samples with RGO contributing to good electronic conductivity, and the lack of a well-connected network in the samples without RGO, leading to poor conductivity as well as a large capacity decay.

2.6 Acknowledgements

We gratefully acknowledge funding from Department of Energy, Office of Basic Energy Sciences, EPSCoR Implementation award DE-SC0007074. We thank Chu Chen for help with the experiments.

2.7 References

1. Liu, C.; Li, F.; Ma, L. P.; Cheng, H. M., Advanced materials for energy storage. *Advanced Materials* **2010,** *22* (8), E28-E62.

2. Tarascon, J.-M.; Armand, M., Issues and challenges facing rechargeable lithium batteries. *Nature* **2001,** *414* (6861), 359-367.

3. Etacheri, V.; Marom, R.; Elazari, R.; Salitra, G.; Aurbach, D., Challenges in the development of advanced Li-ion batteries: a review. *Energy & Environmental Science* **2011,** *4* (9), 3243-3262.

4. Chen, J., Recent progress in advanced materials for lithium ion batteries. *Materials* **2013,** *6* (1), 156-183.

5. Goodenough, J. B.; Park, K.-S., The Li-ion rechargeable battery: a perspective. *Journal of the American Chemical Society* **2013,** *135* (4), 1167-1176.

6. Scrosati, B.; Garche, J., Lithium batteries: Status, prospects and future. *Journal of Power Sources* **2010,** *195* (9), 2419-2430.

7. Noh, M.; Kwon, Y.; Lee, H.; Cho, J.; Kim, Y.; Kim, M. G., Amorphous carbon-coated tin anode material for lithium secondary battery. *Chemistry of materials* **2005,** *17* (8), 1926-1929.

8. Bu, P.; Liu, S.; Lu, Y.; Zhuang, S.; Wang, H.; Tu, F., Effects of carbon back on the electrochemical performance of lithium-organic coordination compound batteries. *Int J Electrochem Sci* **2012,** *7*, 4617-4624.

9. Kim, J.; Kim, B.; Lee, J.-G.; Cho, J.; Park, B., Direct carbon-black coating on LiCoO 2 cathode using surfactant for high-density Li-ion cell. *Journal of power sources* **2005,** *139* (1), 289-294.

10. Fransson, L.; Eriksson, T.; Edström, K.; Gustafsson, T.; Thomas, J. O., Influence of carbon black and binder on Li-ion batteries. *Journal of power sources* **2001,** *101* (1), 1-9.

11. Verdejo, R.; Bernal, M. M.; Romasanta, L. J.; Lopez-Manchado, M. A., Graphene filled polymer nanocomposites. *Journal of Materials Chemistry* **2011,** *21* (10), 3301-3310.

12. Chakraborty, I.; Bodurtha, K. J.; Heeder, N. J.; Godfrin, M. P.; Tripathi, A.; Hurt, R. H.; Shukla, A.; Bose, A., Massive electrical conductivity enhancement of multilayer graphene/polystyrene composites using a nonconductive filler. *ACS applied materials & interfaces* **2014,** *6* (19), 16472-16475.

13. Kim, H.; Abdala, A. A.; Macosko, C. W., Graphene/polymer nanocomposites. *Macromolecules* **2010,** *43* (16), 6515-6530.

14. Larson, R. G., *The Structure and Rheology of Complex Fluids*. Oxford Univ Press: 1999; p 656 pp.

15. Wessel, R., Ball, R.C., Fractal aggregates and gels in shear flow. *Physical Review A* **1992,** *46*, R3008-R3011.

16. Zerda, T. W., Yang, H., Gerspacher, M., Fractal dimension of carbon-black particles. *Rubber chemistry and technology* **1992,** *65*, 130-136.

17. Li, J.; Ma, P.; Sze, C.; Kai, T.; Tang, B.; Kim, J. K. In *Percolation threshold of polymer nanocomposites containing graphite nanoplatelets and carbon nanotubes*, ICCM International Conferences on Composite Materials, 2007.

18. Chen, Y.; Nie, M.; Lucht, B. L.; Saha, A.; Guduru, P. R.; Bose, A., High capacity, stable silicon/carbon anodes for lithium-ion batteries prepared using emulsion-templated directed assembly. *ACS applied materials & interfaces* **2014,** *6* (7), 4678-4683.

19. Saha, A.; Nikova, A.; Venkataraman, P.; John, V. T.; Bose, A., Oil emulsification using surface-tunable carbon black particles. *ACS applied materials & interfaces* **2013,** *5* (8), 3094-3100.

20. Magasinski, A.; Zdyrko, B.; Kovalenko, I.; Hertzberg, B.; Burtovyy, R.; Huebner, C. F.; Fuller, T. F.; Luzinov, I.; Yushin, G., Toward efficient binders for Li-ion battery Si-based anodes: polyacrylic acid. *ACS applied materials & interfaces* **2010,** *2* (11), 3004-3010.

21. Chen, Y.; Xu, M.; Zhang, Y.; Pan, Y.; Lucht, B. L.; Bose, A., All-Aqueous Directed Assembly Strategy for Forming High-Capacity, Stable Silicon/Carbon Anodes for Lithium-Ion Batteries. *ACS applied materials & interfaces* **2015,** *7* (38), 21391-21397.

22. Stone, H.; Brugh, M.; Hopkins, S.; Yoder, H.; Beard, C., Preparation of inactivated oil-emulsion vaccines with avian viral or mycoplasma antigens. *Avian diseases* **1978**, 666-674.

23. Chung, G. C.; Jun, S. H.; Lee, K. Y.; Kim, M. H., Effect of surface structure on the irreversible capacity of various graphitic carbon electrodes. *Journal of The Electrochemical Society* **1999,** *146* (5), 1664-1671.

24. Sharifi-Viand, A.; Mahjani, M.; Jafarian, M., Investigation of anomalous diffusion and multifractal dimensions in polypyrrole film. *Journal of Electroanalytical Chemistry* **2012,** *671*, 51-57.

CHAPTER 3

The Influence of the Oil on the Structure and Electrochemical Performance of Emulsion-Templated Tin/Carbon Anodes for Lithium Ion Batteries

In preparation for *ACS Applied Materials & Interfaces*

Yuzi Zhang[1], Yue Pan[2], Yingnan Dong[2], Brett L. Lucht[2], Arijit Bose[1,*]

[1] Department of Chemical Engineering,

[2] Department of Chemistry, University of Rhode Island, Kingston, Rhode Island, 02881

* Corresponding author: bosea@uri.edu, 401-874-2804

3.1 Abstract

Tin (Sn) is a useful anode material for lithium ion batteries (LIBs) owing to its high theoretical capacity. Emulsion-templating is a simple and scalable technique for preparing anodes for LIBs by forming oil-in-water emulsions with confined active material nanoparticles inside the oil. Carbon black (CB) stabilizes the emulsions as well as forms a conductive network. We fabricated emulsion-templated Sn/CB anodes with octane, hexadecane, 1-chlorohexadecane and 1-bromohexadecane as the oil phase. The vapor pressure and density of the oil affect the drying rates and creaming in the emulsion. The oil droplet size distribution of formed emulsion also has impact on the drying process. All these elements affect the morphology of the dried emulsion, and the electrochemical performance of the anode. Sn/CB anodes prepared with hexadecane (Sn/CB(Hx)) showed a smooth morphology with no cracks, and had the highest capacities and capacity retention. The vapor pressure of hexadecane is low, thus lowering the drying rate and reducing differential stresses on the sample, leading to reduced cracking. Because the density of hexadecane is lower than that of water, creaming forces the emulsion droplets into a close packed arrangement on the surface of the continuous water phase. Smaller oil droplets at the surface also allowed for rapid water evaporation from underneath without damaging the droplets. Upon drying on the current collector, the areal capacity for anodes with creaming are higher than those where the droplets are uniformly dispersed in the emulsions. Therefore, choosing an appropriate oil is helpful in obtaining the best cell performance for emulsion-templated anodes for use in LIBs.

3.2 Introduction

Lithium ion batteries (LIBs) with high energy density and long cycle life are important for advanced electronic devices and electric vehicles.[1-6] Among a variety of anode materials for LIBs, tin (Sn) has been regarded as one of the most promising candidates due to its high theoretical specific capacity of 994 mAh/g, and the highest volumetric energy density of 7262 mAh/cm^3.[7-8] However, a major drawback is that Sn undergoes a dramatic volume change of around 300% during lithiation/delithiation, resulting in fracture and pulverization, contact loss with conductive carbon agents and the current collector, as well as the continuous formation of a solid electrolyte interphase (SEI) that consumes lithium ions. All these mechanisms contribute to capacity fading and low Coulombic efficiencies.[9-11]

Sn nanoparticles,[12-13] porous Sn nanostructures,[14-15] core-shell Sn-carbonaceous configurations,[7, 16-18] and Sn-graphene nanocomposites have been used for making Sn-based anodes.[19-20] These configurations are designed to accommodate volume changes of Sn during lithiation/delithiation, leading to superior cycle performance.

Previously, we reported an emulsion-templated approach for preparing silicon (Si)-based anodes for LIBs.[21] Si nanoparticles (SiNPs) were confined in octane droplets stabilized by carbon black (CB), which also formed a porous CB cage surrounding the SiNPs. There was enough available room within these cages to allow for volume expansion and contraction of the SiNPs during lithiation/delithiation without transmitting these strains to the surrounding carbon black network. Spatial variations of stress during lithiation and delithiation are small over the dimensions of the nanoparticles, thus avoiding pulverization. This Si/CB anode exhibited excellent

cycle performance with capacity retention of 67% after 50 cycles at a cycle rate of 0.1C.

The oil phase is an important component in this colloidal-based strategy. It can have different densities and vapor pressures. The former has a direct impact on whether the emulsion creams. The latter has a strong impact on drying rates at a fixed temperature.[22-23] Different oils can also lead to distinct droplet size distributions of the formed emulsions. All of these can impact the morphology of the dried anode. In this paper, we extend the emulsion-templating approach to prepare Sn nanoparticle (SnNP) based anodes using various oils. We investigate the effect of the oil on the morphology, and the electrochemical performance for the emulsion-templated Sn-based anodes.

3.3 Experiments

3.3.1 Preparation of anodes

SnNPs (average diameter ~60-80 nm) were purchased from US Research Nanomaterials Incorporation. The para-amino benzoic acid-terminated CB suspension in water at pH 7.5 was provided by Cabot Corporation. The CB particles are fractal and have a specific surface area of ~200 m^2/g. At neutral pH, the carboxyl groups on CB are deprotonated. These CB particles are highly hydrophilic and are stably suspended in water. The oils used in this work were octane (99%), hexadecane (99%), 1-chlorohexadecane (95%) and 1-bromohexadecane (97%), purchased from Sigma Aldrich. Their densities at 25°C and vapor pressures at 50°C of all the oils are shown in Table I. All oils were used as received. Sn has a density of 7.3 gm/cc, making it challenging to disperse in the oil. Our calculations reveal that Brownian motion will

dominate over sedimentation so long as the particle diameter is less than 360 nm. These particles may however, aggregate during drying. Deionized water was obtained from a Millipore Milli Q system.

Table I. Physical properties for different liquids [24-27]

	Formula	Density at 25°C (g/ml)	Vapor pressure at 50°C (KPa)
Octane (Oct)	$CH_3(CH_2)_6CH_3$	0.703	6.04
Hexadecane (Hx)	$CH_3(CH_2)_{14}CH_3$	0.770	0.00253
1-Chlorohexadecane (ClHx)	$CH_3(CH_2)_{15}Cl$	0.865	0.000311
1-Bromohexadecane (BrHx)	$CH_3(CH_2)_{15}Br$	0.999	0.000133
Water	H_2O	0.997	12.3

The Sn/CB anode was prepared by the emulsion-templated method shown in Figure 3.1. 1M hydrochloric acid (HCl) was added to a 1% w/w CB suspension, and the pH was adjusted to ~3.3. The addition of the acid protonates some of the surface carboxylate groups on CB, increasing their hydrophobicity. These partially hydrophobic particles, reside at the oil-water interfaces, as well as form a connected network in aqueous phase.[28]

A 1.5% w/v suspension of SnNPs in each oil was sonicated for 1 hour, and then mixed with the acid-mediated CB suspension by vortexing for 3 min at 3000 rpm. The volume ratio of the SnNPs/oil suspension to the CB/water suspension was 2:3. The mass ratio of SnNPs to CB was 1:1. An oil-in-water emulsion was formed after vortexing. A 40 mg/ml aqueous binder solution containing polyvinyl alcohol (PVA) and carboxymethyl cellulose (CMC) at a 1:1 weight ratio was added to the emulsion and vortexed for 5 min. The volume of the PVA/CMC solution was adjusted so that the final concentration of binder was 20 wt% of the dried anode mass consisting of Sn, CB and binder. The emulsion was then transferred onto a CR2032 coin cell and dried

overnight at 50°C under a vacuum. These anode preparation conditions were repeated for all the four oils. The areal loading on the coin cell was ~1.5 mg/cm^2. The dried Sn/CB anodes prepared with octane, hexadecane, 1-chlorohexadecane and 1-bromohexadecane were labeled as Sn/CB(Oct), Sn/CB(Hx), Sn/CB(ClHx) and Sn/CB(BrHx), respectively.

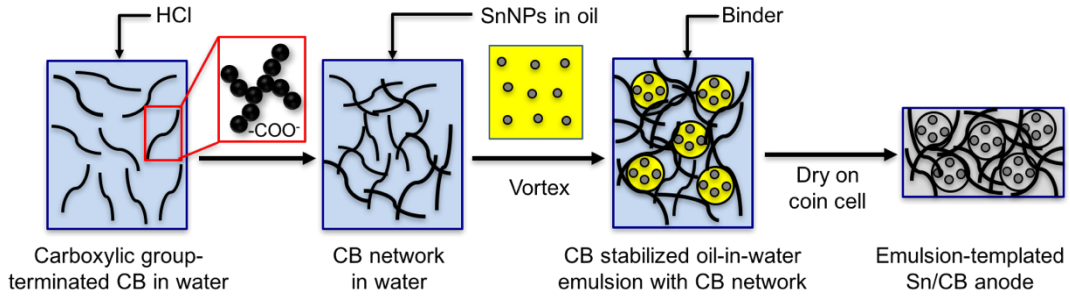

Figure 3.1. Schematic showing the preparation of the emulsion-templated Sn/CB anodes. 1 M HCl was added to an aqueous carboxyl-terminated CB suspension until the pH reached 3.3. SnNPs, suspended in an oil, were then added to the CB suspension. The mixture was vortexed to form oil-in-water emulsions. After adding a binder solution, the emulsion was placed on a coin cell and dried to produce the Sn/CB anodes. Octane, hexadecane, 1-chlorohexadecane and 1-bromohexadecane were used as the oils.

3.3.2 Electrochemical characterization

CR2032 coin cells were assembled in an argon-filled glovebox (H_2O <1 ppm, O_2 <0.1 ppm) with metallic Li foil employed as the counter electrode. The electrolyte was a mixture of 1.0 M $LiPF_6$ in ethylene carbonate (EC) / diethyl carbonate (DEC) / fluoroethylene carbonate (FEC) at a ratio of 45:45:10 by volume. The battery grade Li salt and electrolytes were obtained from BASF. A polypropylene microporous membrane, Celgard 2325, and one glass fiber membrane were used as the separators. Galvanostatic (constant current) charge/discharge cycling tests were conducted on a BST8-WA battery cycler (5 V/1 mA) at room temperature, with a cycle rate of 0.05C (current density of ~ 30 μA/cm^2) for the first 4 cycles followed by 0.2C (current

density of ~120 $\mu A/cm^2$) for the remaining cycles, for a total of 50 cycles, over the potential range of 0.05-3 V vs. Li^+/Li.

3.3.3 Morphological characterization

Fresh Sn/CB emulsions prepared with various oils were observed by bright-field optical microscopy in a Nikon Eclipse E 600 microscope. Image-J was used to process the emulsion images for ~200 droplets to obtain average droplet sizes and droplet size distributions. The emulsions were also imaged using cryogenic scanning electron microscopy (cryo-SEM) using a Gatan Alto 2500 cryo preparation system attached to a Zeiss Sigma VP field emission scanning electron microscope, operating at 2 kV. The sample was maintained at -130°C during imaging. The uncycled dried Sn/CB emulsions were imaged using SEM at 10 kV to investigate the surface morphology of anodes, and elemental maps were created using selected area energy dispersive spectroscopy (EDS) to examine the spatial distribution of Sn and C. Transmission electron microscopy (TEM) was employed to characterize the cycled Sn/CB anodes after 50 cycles using a JEOL 2100 transmission electron microscope. After cell disassembly, we put a small piece of the electrode in dimethyl carbonate and dispersed it using sonication. Then a drop of the dispersion was placed on a TEM grid and dried under vacuum. The grid was stored in an argon-filled vial until it was observed by TEM. Selected area electron diffraction (SAED) was performed on regions of interest of the samples to obtain phase information.

3.4 Results and discussion

A drop of water or oil was added to the emulsion. The water drop spread out immediately, but the oil drop did not, confirming that we always had oil-in-water

emulsions. Figure 3.2 shows optical microscopic images and size distributions of Sn/CB emulsions prepared with four oils. The average droplet sizes for the emulsions are 40, 32, 51 and 43 μm, respectively, corresponding to the oil phases of octane, hexadecane, 1-chlorohexadecane and 1-bromohexadecane. Among all the emulsions, Sn/CB(Hx) have the smallest droplets with a narrower size distribution and a smaller average droplet diameter.

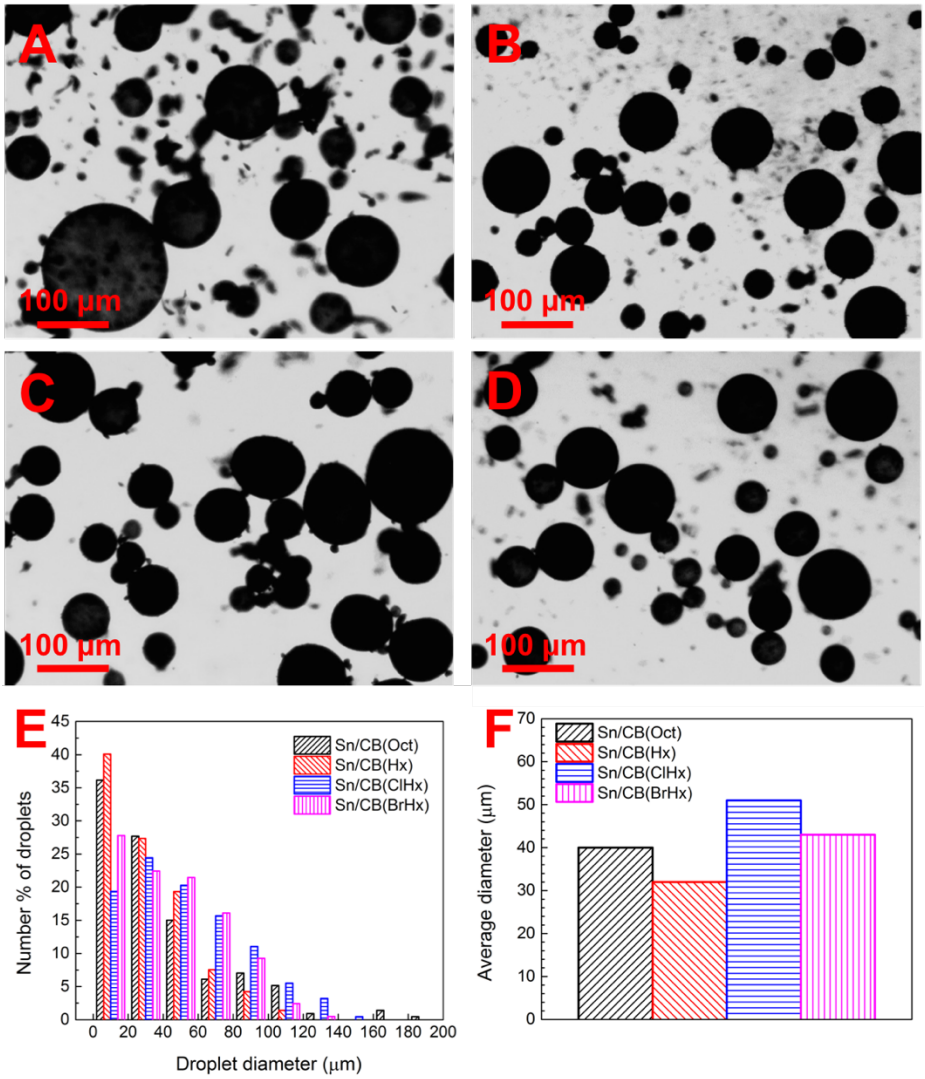

Figure 3.2. Optical microscopic images of fresh Sn/CB emulsions prepared with four oils. (A) Sn/CB(Oct), (B) Sn/CB(Hx), (C) Sn/CB(ClHx), (D) Sn/CB(BrHx). (E) Droplet size distributions of four emulsions with different oil phases. (F) Average diameter for each class of emulsion droplets. In E and F, Sn/CB(Hx) emulsions have the smallest droplets among all four emulsions.

Figure 3.3A is a cryo-SEM image of a droplet in the Sn/CB(BrHx) emulsion. In the magnified images (Figures 3.3B-3.3D), CB particles residing at the oil-water interface stabilized the emulsion, and SnNPs confined in the oil phase are seen. Some CB particles in the aqueous phase formed a connected network.[29] A SEM image of a dried droplet from a Sn/CB(BrHx) anode is shown in Figure 3.3E. Elemental mapping of Figure 3.3E revealed that the SnNPs were mostly confined inside the 'oil' region, and CB-rich region was the dried aqueous phase (Figure 3.3F).

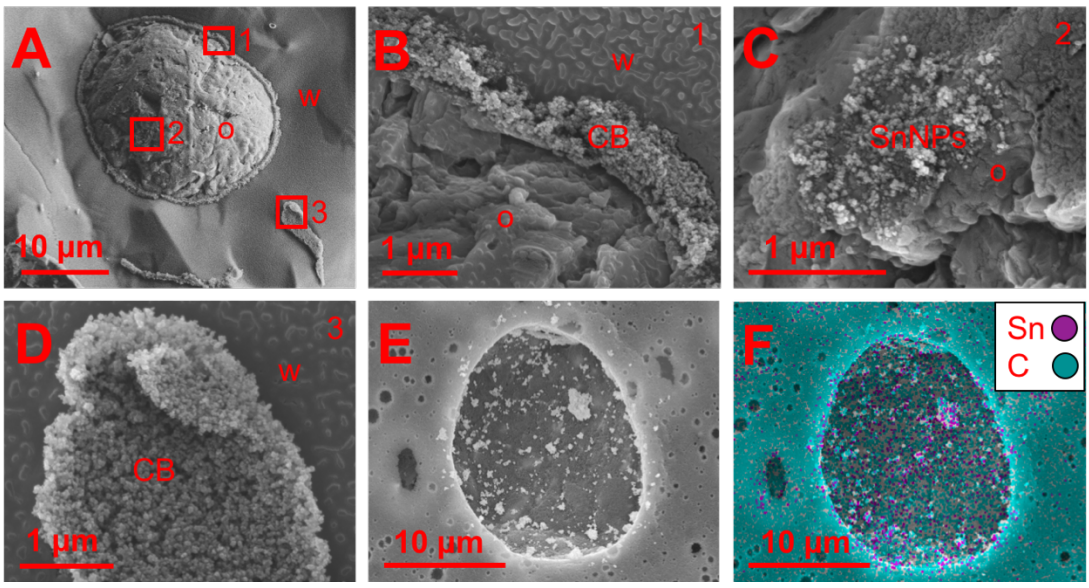

Figure 3.3. (A) A cryo-SEM image of the Sn/CB(BrHx) emulsion shows an oil-in-water droplet. The magnified areas are shown in (B), (C) and (D). (B) CB particles residing at the oil-water interface stabilized the emulsion. (C) SnNPs were confined in the oil phase. (D) CB particles formed aggregates in the aqueous phase. (E) A SEM image of the dried Sn/CB(BrHx) emulsion. (F) An elemental map of C and Sn in Figure E. Most SnNPs were confined in the regions previously occupied by the oil, while carbon was mostly distributed outside the Sn-rich regions.

Figure 3.4A is a SEM image for Sn/CB(Oct) sample, where a rough and porous structure was observed. The Sn/CB(Hx) sample (Figure 3.4B) showed a more smooth and homogeneous surface with few defects indicating good integrity of the structure after drying the emulsion. In the dried Sn/CB(ClHx) sample (Figure 3.4C), significant

voids with dimensions of the order of a few hundred microns were observed in the regions occupied by oil. Some of these voids resembled the dried flocculated or coalesced droplets during the drying process. For the Sn/CB(BrHx) sample shown in Figure 3.4D, similar large voids were observed at the previous droplet regions. The morphology of these voids also suggested some possible droplet flocculation and coalescence upon drying. Some of the dried droplets were exposed at the surface, while others were underneath the surface. This was because 1-bromohexadecane and water are nearly equal in density, and thus the droplets were distributed throughout the aqueous phase in the oil-in-water emulsion, as shown in Figure 3.4E. Significant creaming was observed in the other samples where the densities of these oils are smaller than water (Figure 3.4E).

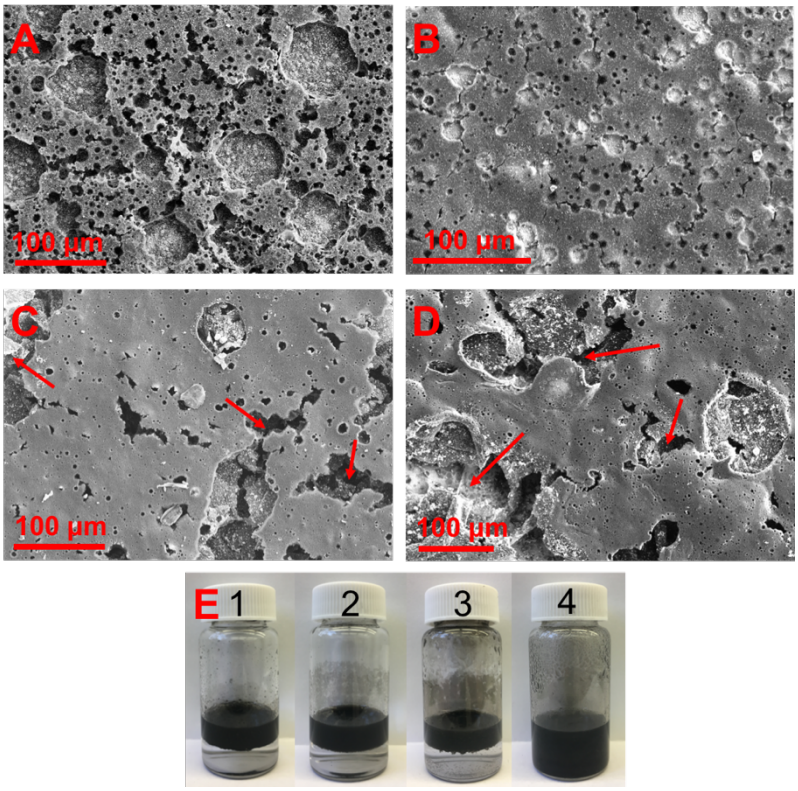

Figure 3.4. SEM images of the dried Sn/CB emulsions prepared with four oils. (A) Sn/CB(Oct). Sample has a rough surface with small pores and cracks. (B) Sn/CB(Hx).

Sample surface is smooth with few small flaws. (C) Sn/CB(ClHx). Large voids are visible in the sample, but the rest of the sample is smooth. In A, B and C, the dried droplets regions always remained at the surface due to the lower densities of these oils in oil-in-water emulsions. (D) Sn/CB(BrHx). Sample surface has large voids. Red arrows in C and D indicate the occurrence of large voids in the samples. (E) A demonstration of oil-in-water emulsions shows creaming in the samples labeled as 1, 2, 3, corresponding to octane, hexadecane, and 1-chlorohexadecane as the oil phases, and non-creaming for the sample labeled as 4, where the oil is 1-bromohexadecane.

The vapor pressure and density of the oils, as well as the droplet size distributions of the prepared emulsions, all play important roles in determining the morphology of the dried emulsions. At 50°C, octane has a vapor pressure that is slightly lower than water, hence the evaporation rates of octane and water are similar. The consequence after drying was a porous structure of the dried emulsion due to the large induced stress resulting from the rapid evaporation of oil and water. For hexadecane, 1-chlorohexadecane and 1-bromohexadecane, their vapor pressures are significantly smaller than water in a few orders of magnitude. Therefore, in the drying process, all of the three oils underwent much slower evaporation comparably. Creaming of the emulsions prepared with hexadecane and 1-chlorohexadecane caused the oil droplets to rise to the water surface. As mentioned above, Sn/CB(Hx) emulsions had smaller droplets than the others. In the drying step, these small oil droplets remained at the water surface with slow evaporation. The packing of small droplets led to a large number of short connected ‘channels’ in between, which allowed the water underneath to evaporate rapidly without disrupting the oil droplets. The volume of the aqueous phase shrank after drying. This resulted in a smooth and dense morphology of the dried emulsion. For 1-chlorohexadecane, the oil droplets with larger size packed at the water surface and evaporated slowly. However, the space between the packed droplets

was less compared to that of hexadecane, which hindered the evaporation of water. Meanwhile, some droplets formed aggregation. Upon drying, all these factors contributed to a rough structure with significant voids, in the previous aggregated droplet regions as well as some cracks. For 1-bromohexadecane, the oil droplets are suspended throughout the emulsion. With water evaporation around the droplets, the sample underwent some shrinkage causing partial droplet flocculation. These flocculated oil drops then became big voids after drying, and showed an unevenly porous structure in the dried emulsion. We believe these distinct morphologies of the dried Sn/CB emulsions influence their cycle performance.

The electrochemical performance of the Sn/CB containing anodes prepared with the four oils are shown in Figure 3.5. They represent an average from 3 different cells, and the error bars indicate the maximum spread in the data. Figure 3.5A shows the specific delithiation capacities of the Sn/CB anodes. All capacities were calculated based on the total mass of Sn, CB and binder. Sn/CB(Hx) anodes showed the highest capacities, with an initial capacity of 484 mAh/g and a capacity of 327 mAh/g after cycling. Sn/CB(Oct) anodes had a similar initial capacity of 469 mAh/g to that of Sn/CB(Hx), however, as cycling continued, the capacity dropped rapidly, ending up with only 169 mAh/g after 50 cycles. The initial capacities of Sn/CB(ClHx) and Sn/CB(BrHx) anodes were 297 mAh/g and 218 mAh/g, respectively, indicating that the number of SnNPs involved in the first delithiation process was significantly reduced compared to those of Sn/CB(Hx) and Sn/CB(ClHx) anodes. The Sn/CB(BrHx) anodes showed the lowest capacities at all times during cycling. The low capacities of Sn/CB(ClHx) and Sn/CB(BrHx) anodes had a strong dependence on their rough structures. The possible

reason could be that the pre-existing significant voids and cracks in these anodes impaired the electrical contact between some of the active materials and the conductive agent as well as the current collector. Therefore, a significant number of SnNPs were not available for Li ion insertion/extraction even at the beginning of the cycling.

We allowed for initial SEI formation by using charge/discharge rates of 0.05C for the first 4 cycles. The capacity retentions of all the anodes from the 5th cycle onwards, where we used charge/discharge rates of 0.2C, normalized by their respective capacities at the end of the 5th cycle, are shown in Figure 3.5B. Amongst all the Sn-based anodes, Sn/CB(Hx) underwent the least capacity fading with retention of 77% at the end of cycling. This was consistent with the dense and crack-free morphology of Sn/CB(Hx) anodes. A dramatic capacity drop was observed in the Sn/CB(Oct) anodes, with capacity retention of only 45% after 50 cycles. Sn/CB(ClHx) and Sn/CB(BrHx) anodes showed relatively higher capacity retention of 67% and 59% due to their low capacity values at the 5th cycle. The drastic capacity decay in Sn/CB(Oct), Sn/CB(ClHx) and Sn/CB(BrHx) anodes possibly resulted from their porous morphologies with significant voids. These structural flaws contributed to an increase in the anode surface area that was exposed to the electrolyte, potentially resulting in further SEI formation at these regions, where irreversible reactions occurred consuming Li ions.[30] Due to the induced stress caused by volume change during Li ion insertion/extraction, the existing cracks in the anodes may also propagate with cycling. This can potentially promote delamination and peeling of the electrode, leading to the

isolation of active materials from the current collector, namely, loss of electrical contact.[31-32] All the above mechanisms eventually resulted in loss of capacity. Figures 3.5C and 3.5D show the voltage –specific capacity profiles for Sn/CB anodes over the range of 0.05-3V for the 1st and 50th cycle. In Figure 3.5C, Sn/CB(Hx) anodes had the highest delithiation capacity but the lithiation capacity was low, leading to the highest initial efficiency of 61%, which suggested more reversible reactions occurring in the first cycle. The low initial efficiencies for all the Sn/CB anodes were associated with SEI formation.[33] After 50 cycles (Figure 3.5D), the efficiency for Sn/CB(Hx) anodes reached ~98%, higher than those of other anodes. Similar low efficiencies for Sn anodes can be found in the literature.[20, 34]

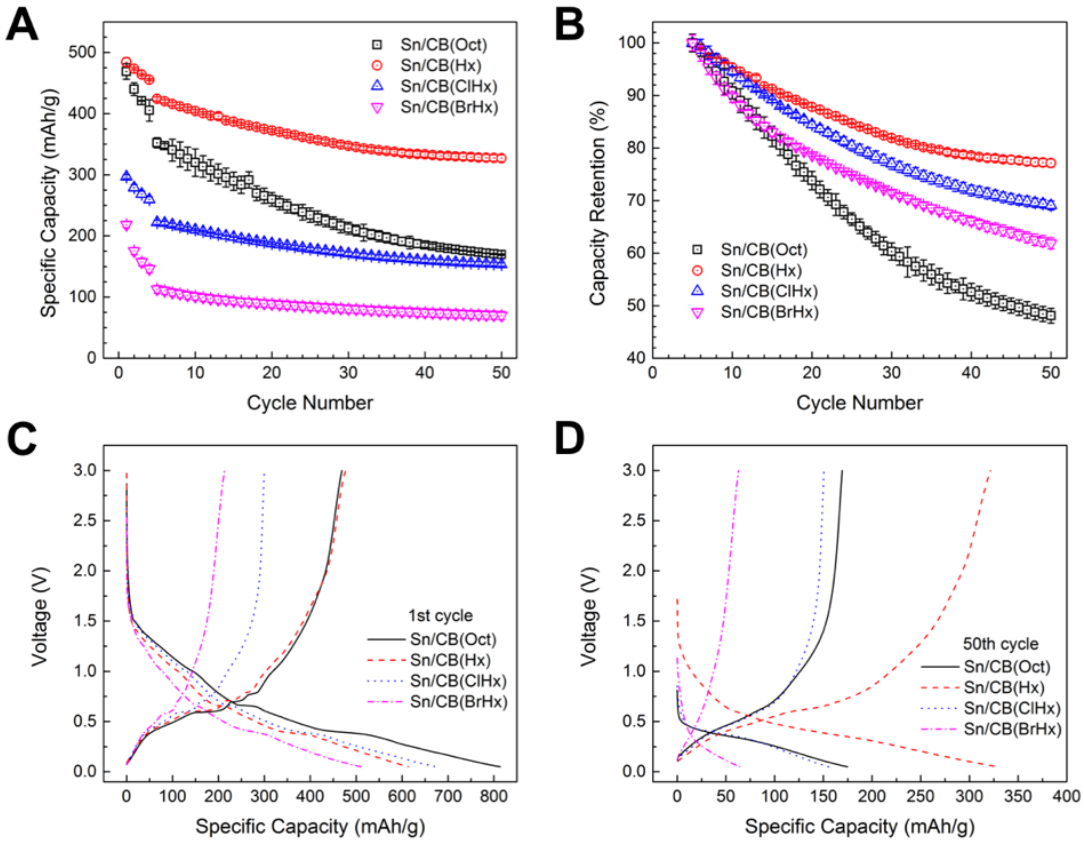

Figure 3.5. Electrochemical characterization of the emulsion-templated Sn/CB anodes prepared with four oils, at a charge/discharge rate of 0.05C for the first 4 cycles followed by 0.2C for 46 cycles. (A) Delithiation capacity, (B) Delithiation capacity

retention (normalized by their respective capacities at the 5th cycle), (C) Voltage-specific capacity profiles over the range of 0.05-3.0 V (versus Li/Li^+) for the 1st cycle and (D) the 2nd cycle. The data represent average values from 3 runs. The error bars indicate the maximum spread in the data.

For specific capacity, capacity retention and efficiency, Sn/CB(Hx) anodes showed the best electrochemical performance amongst all the Sn/CB anodes. This was consistent with their crack-free morphology that was advantageous for Li ion insertion/extraction. All these results indicated the selection of oil was important to the cell performance as it determined the final structure of the dried emulsion, which correlated with the electrochemical performance.

To investigate the mechanisms of lithiation/delithiation process, we examined the differential capacity dQ/dV curves for the 1st and 2nd cycle for all Sn/CB anodes between 0.05 and 3V (Figures 3.6A and 3.6B). In the 1st cycle (Figure 3.6A), two sharp cathodic peaks at approximately 0.38 and 0.66 V were observed for all Sn/CB anodes which can be assigned to the two-step lithiation of Sn with Li to form Li_xSn ($x \leq 4.4$) alloy.[16, 35-36] In the anodic cycle, four oxidation peaks at around 0.46, 0.61, 0.71 and 0.79 V corresponded to the delithiation reaction of Li_xSn alloy.[16, 37] In the 2nd cycle (Figure 3.6B), all the above peaks occurred with no obvious shifting in potential. However, a small reduction peak at 1.0 V was observed in the 1st cycle but disappeared afterwards, we proposed that it was representative of the SEI formation. A very broad anodic peak occurred at 1.0 V in the 1st and 2nd cycle, which can be attributed to the Li extraction from the carbon.[14, 17] Although Sn/CB(ClHx) and Sn/CB(BrHx) anodes both showed very low capacities, we did not see any side reactions. The difference in peak intensities on the dQ/dV curves for all Sn/CB

anodes, was consistent with their cycle performance. All of these results were correlated with the unique structures of Sn/CB anodes prepared using various oils.

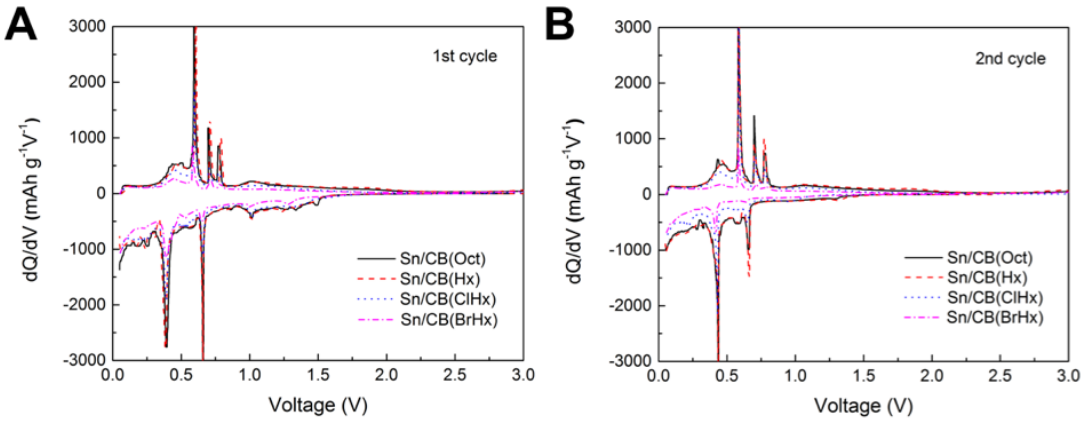

Figure 3.6. Differential capacity dQ/dV curves of Sn/CB anodes prepared with four oils for (A) the 1st cycle and (B) the 2nd cycle.

The morphology of anodes after cycling was observed by TEM. After 50 cycles, as shown in Figures 3.7A, 3.7C and 3.7D, SnNPs in Sn/CB(Oct), Sn/CB(ClHx) and Sn/CB(BrHx) anodes suffered severe pulverization and lost their distinctive spherical morphology. For Sn/CB(Hx) anode, the spherical shape of SnNPs was retained showing clearly visible edges (Figure 3.7B). SAED images of uncycled SnNPs and cycled SnNPs in all Sn/CB anodes are shown in Figure 3.8. All images showed diffuse diffraction patterns, suggesting that SnNPs before and after cycling had amorphous structures. The cycling process did not cause any phase change of SnNPs. These results indicated that the structural features of Sn/CB(Hx) anode significantly reduced SnNPs fracturing and pulverization.

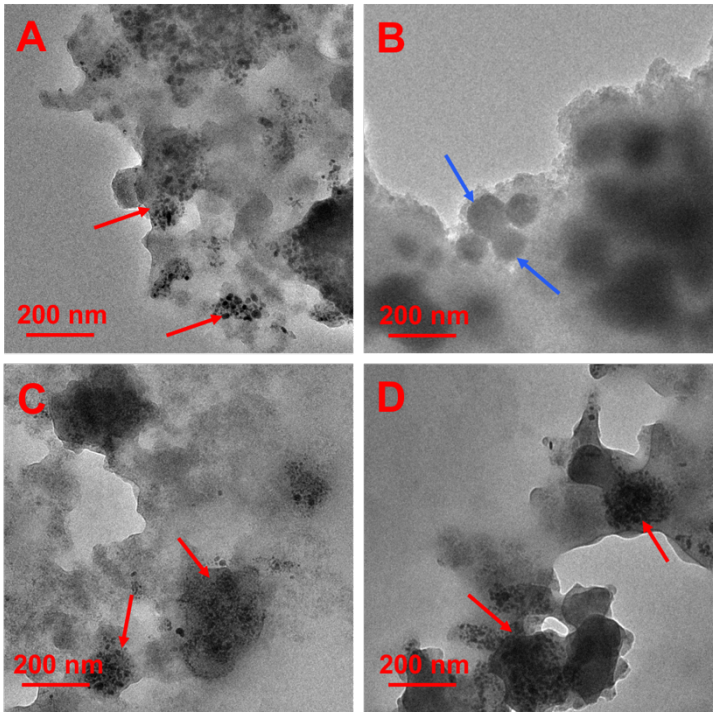

Figure 3.7. TEM images of the Sn/CB anodes prepared with four oils after cycling. (A) Sn/CB(Oct). (B) Sn/CB(Hx). (C) Sn/CB(ClHx). (D) Sn/CB(BrHx). In A, C and D, red arrows indicate the pulverized SnNPs in the samples. While In B, blue arrows indicate the whole SnNPs.

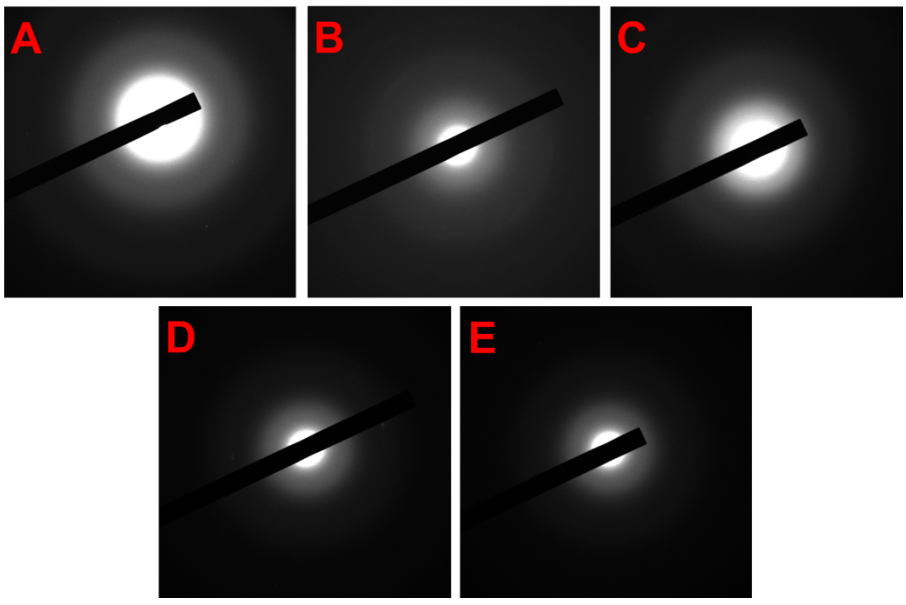

Figure 3.8. SAED images of (A) uncycled SnNPs and cycled SnNPs for anodes of (B) Sn/CB(Oct), (C) Sn/CB(Hx), (D) Sn/CB(ClHx), (E) Sn/CB(BrHx). All images show diffuse diffraction pattern, indicating an amorphous structure of SnNPs in each sample.

3.5 Conclusions

We fabricated Sn-based anodes for LIBs utilizing a simple emulsion-templating strategy with different oils. We investigated the effect of oil on the morphology and the electrochemical performance for the Sn/CB anodes. As hexadecane has a smaller density and a significantly lower vapor pressure than water, the evaporation rate of hexadecane is much reduced during drying process. Smaller oil droplets of Sn/CB(Hx) emulsions remaining at the water surface allowed water underneath to evaporate rapidly without disrupting the oil droplets. All of these elements contributed to a dense and homogenous morphology with few flaws for dried Sn/CB(Hx) samples compared to those prepared using other oils. Sn/CB(Hx) anodes showed the highest specific delithiation capacities and the highest capacity retention throughout 50 cycles. The poor cycle performance of Sn/CB(Oct), Sn/CB(ClHx) and Sn/CB(BrHx) anodes can be attributed to their structural disintegration showing significant voids and cracks. These results indicate that the choice of the oil is very important in the emulsion-templating technique for forming anodes for LIBs.

3.6 Acknowledgements

We gratefully acknowledge funding from Department of Energy, Office of Basic Energy Sciences, EPSCoR Implementation award DE-SC0007074.

3.7 References

1. Goodenough, J. B.; Kim, Y., Challenges for rechargeable Li batteries. *Chemistry of Materials* **2009,** *22* (3), 587-603.

2. Balsara, N. P.; Newman, J., Comparing the energy content of batteries, fuels, and materials. *Journal of Chemical Education* **2013,** *90* (4), 446-452.

3. Goodenough, J. B.; Park, K.-S., The Li-ion rechargeable battery: a perspective. *Journal of the American Chemical Society* **2013,** *135* (4), 1167-1176.

4. Horiba, T., Lithium-ion battery systems. *Proceedings of the IEEE* **2014,** *102* (6), 939-950.

5. Chen, H.; Cong, T. N.; Yang, W.; Tan, C.; Li, Y.; Ding, Y., Progress in electrical energy storage system: A critical review. *Progress in Natural Science* **2009,** *19* (3), 291-312.

6. Tao, H.; Feng, Z.; Liu, H.; Kan, X.; Chen, P., Reality and future of rechargeable lithium batteries. *Open Materials Science Journal* **2011,** *5* (1), 204-214.

7. Li, N.; Song, H.; Cui, H.; Yang, G.; Wang, C., Self-assembled growth of Sn@ CNTs on vertically aligned graphene for binder-free high Li-storage and excellent stability. *Journal of Materials Chemistry A* **2014,** *2* (8), 2526-2537.

8. Li, J.; Yang, F.; Ye, J.; Cheng, Y.-T., Whisker formation on a thin film tin lithium-ion battery anode. *Journal of Power Sources* **2011,** *196* (3), 1474-1477.

9. Wang, B.; Luo, B.; Li, X.; Zhi, L., The dimensionality of Sn anodes in Li-ion batteries. *Materials today* **2012,** *15* (12), 544-552.

10. Tian, H.; Xin, F.; Wang, X.; He, W.; Han, W., High capacity group-IV elements (Si, Ge, Sn) based anodes for lithium-ion batteries. *Journal of Materiomics* **2015,** *1* (3), 153-169.

11. Kamali, A. R.; Fray, D. J., Tin-based materials as advanced anode materials for lithium ion batteries: a review. *Rev. Adv. Mater. Sci* **2011,** *27* (1), 14-24.

12. Qu, J.; YonganYang; ZhihuiChen; YurongRen; JianningDing; NingyiYuan, A Facile Hydrothermal Synthesis of Ultrasmall Sn Nanoparticles in Carbon Matrices as

Anode for Lithium Ion Battery. *INTERNATIONAL JOURNAL OF ELECTROCHEMICAL SCIENCE* **2016,** *11* (6), 4389-4398.

13. Zhang, W. M.; Hu, J. S.; Guo, Y. G.; Zheng, S. F.; Zhong, L. S.; Song, W. G.; Wan, L. J., Tin-nanoparticles encapsulated in elastic hollow carbon spheres for high-performance anode material in lithium-Ion batteries. *Advanced Materials* **2008,** *20* (6), 1160-1165.

14. Xu, Y.; Guo, J.; Wang, C., Sponge-like porous carbon/tin composite anode materials for lithium ion batteries. *Journal of Materials Chemistry* **2012,** *22* (19), 9562-9567.

15. Wang, Y.; Xu, M.; Peng, Z.; Zheng, G., Direct growth of mesoporous Sn-doped TiO 2 thin films on conducting substrates for lithium-ion battery anodes. *Journal of Materials Chemistry A* **2013,** *1* (42), 13222-13226.

16. Xu, Y.; Liu, Q.; Zhu, Y.; Liu, Y.; Langrock, A.; Zachariah, M. R.; Wang, C., Uniform nano-Sn/C composite anodes for lithium ion batteries. *Nano letters* **2013,** *13* (2), 470-474.

17. Jung, Y. S.; Lee, K. T.; Ryu, J. H.; Im, D.; Oh, S. M., Sn-carbon core-shell powder for anode in lithium secondary batteries. *Journal of the Electrochemical Society* **2005,** *152* (7), A1452-A1457.

18. Seo, S.-D.; Lee, G.-H.; Lim, A.-H.; Min, K.-M.; Kim, J.-C.; Shim, H.-W.; Park, K.-S.; Kim, D.-W., Direct assembly of tin–MWCNT 3D-networked anode for rechargeable lithium ion batteries. *RSC Advances* **2012,** *2* (8), 3315-3320.

19. Wang, C.; Li, Y.; Chui, Y.-S.; Wu, Q.-H.; Chen, X.; Zhang, W., Three-dimensional Sn–graphene anode for high-performance lithium-ion batteries. *Nanoscale* **2013,** *5* (21), 10599-10604.

20. Wang, G.; Wang, B.; Wang, X.; Park, J.; Dou, S.; Ahn, H.; Kim, K., Sn/graphene nanocomposite with 3D architecture for enhanced reversible lithium storage in lithium ion batteries. *Journal of Materials Chemistry* **2009,** *19* (44), 8378-8384.

21. Chen, Y.; Nie, M.; Lucht, B. L.; Saha, A.; Guduru, P. R.; Bose, A., High capacity, stable silicon/carbon anodes for lithium-ion batteries prepared using emulsion-templated directed assembly. *ACS applied materials & interfaces* **2014,** *6* (7), 4678-4683.

22. van Wesenbeeck, I.; Driver, J.; Ross, J., Relationship between the evaporation rate and vapor pressure of moderately and highly volatile chemicals. *Bulletin of environmental contamination and toxicology* **2008,** *80* (4), 315-318.

23. Mackay, D.; van Wesenbeeck, I., Correlation of chemical evaporation rate with vapor pressure. *Environmental science & technology* **2014,** *48* (17), 10259-10263.

24. Li, J. C.; Rossini, F. D., Vapor Pressures and Boiling Points of the l-Fluoroalkanes, l-Chloroalkanes, l-Bromoalkanes, and l-Iodoalkanes, C1to C20. *Journal of Chemical and Engineering Data* **1961,** *6* (2), 268-270.

25. Lide, D. R., Handbook of chemistry and physics. CRC press Boca Raton, FL: 2004.

26. Peisheng, Y. S. M.; Yongsi, R., DETERMINATION OF VERY LOW VAPOR PRESSURES OF SEVEN ORGANIC COMPOUNDS. *Journal of Chemical Industry and Engineering (China)* **1994,** *1*, 015.

27. Willingham, C. B.; Taylor, W.; Pignocco, J. M.; Rossini, F., Vapor pressures and boiling points of some paraffin, alkylcyclopentane, alkylcyclohexane, and alkylbenzene hydrocarbons. *Journal of Research of the National Bureau of Standards* **1945,** *35* (3), 219-244.

28. Saha, A.; Nikova, A.; Venkataraman, P.; John, V. T.; Bose, A., Oil emulsification using surface-tunable carbon black particles. *ACS applied materials & interfaces* **2013,** *5* (8), 3094-3100.

29. Zhang, Y.; Pan, Y.; Chen, Y.; Lucht, B. L.; Bose, A., Towards reducing carbon content in silicon/carbon anodes for lithium ion batteries. *Carbon* **2017,** *112*, 72-78.

30. Verma, P.; Maire, P.; Novák, P., A review of the features and analyses of the solid electrolyte interphase in Li-ion batteries. *Electrochimica Acta* **2010,** *55* (22), 6332-6341.

31. Agubra, V.; Fergus, J., Lithium ion battery anode aging mechanisms. *Materials* **2013,** *6* (4), 1310-1325.

32. Teki, R.; Datta, M. K.; Krishnan, R.; Parker, T. C.; Lu, T. M.; Kumta, P. N.; Koratkar, N., Nanostructured silicon anodes for lithium ion rechargeable batteries. *Small* **2009,** *5* (20), 2236-2242.

33. Chung, G. C.; Jun, S. H.; Lee, K. Y.; Kim, M. H., Effect of surface structure on the irreversible capacity of various graphitic carbon electrodes. *Journal of The Electrochemical Society* **1999,** *146* (5), 1664-1671.

34. Agubra, V. A.; Zuniga, L.; De la Garza, D.; Gallegos, L.; Pokhrel, M.; Alcoutlabi, M., Forcespinning: A new method for the mass production of Sn/C composite nanofiber anodes for lithium ion batteries. *Solid State Ionics* **2016,** *286*, 72-82.

35. Li, Z.; Lv, W.; Zhang, C.; Qin, J.; Wei, W.; Shao, J.-J.; Wang, D.-W.; Li, B.; Kang, F.; Yang, Q.-H., Nanospace-confined formation of flattened Sn sheets in pre-seeded graphenes for lithium ion batteries. *Nanoscale* **2014,** *6* (16), 9554-9558.

36. Wang, Y.; Wu, M.; Jiao, Z.; Lee, J. Y., Sn@ CNT and Sn@ C@ CNT nanostructures for superior reversible lithium ion storage. *Chemistry of Materials* **2009,** *21* (14), 3210-3215.

37. Deng, D.; Lee, J. Y., Reversible storage of lithium in a rambutan‐like tin–carbon electrode. *Angewandte Chemie International Edition* **2009,** *48* (9), 1660-1663.

CHAPTER 4

Microstructures and Rheological Behavior for Aqueous Suspensions of Carbon Black and Mixtures of Carbon Black and Reduced Graphene Oxide

In preparation for *Colloids and Surfaces A: Physicochemical and Engineering Aspects*

Yuzi Zhang, Joe Sullivan, Arijit Bose*

Department of Chemical Engineering, University of Rhode Island, Kingston, Rhode Island, 02881

* Corresponding author: bosea@uri.edu, 401-874-2804

4.1 Abstract

The influence of pH between 3 and 7.5, for carbon black (CB) aqueous suspensions for a range of CB concentrations from 0.05wt% to 10wt% was investigated. Microstructures by cryogenic Scanning Electron Microscopy (cryo-SEM) showed CB particles formed aggregates and transient network from low to high CB concentrations at pH 3. CB above 0.5wt% showed a viscosity increase and shear thinning behavior at pH 3. Addition of reduced graphene oxide (RGO) at 0.05wt% resulted in a viscosity increase of the mixed suspensions for CB between 0.5wt% and 1.5wt%. RGO in these conditions formed connections with CB particles which were beneficial for partial network formation. However, this structural transition was not sufficient to cause any change in moduli of the whole sample.

4.2 Introduction

Carbon black (CB) and reduced graphene oxide (RGO) both belong to the carbon family with shared properties such as high surface area and excellent electrical conductivity, resulting in wide-spread laboratory research study and industrial applications. As a basic material with a long history, CB has been applied into many commercial products including tires,[1-3] ink and paints,[4-6] and plastics,[7-9] working as a reinforcing, coloring, or conductive agent, respectively. Newly developed fields such as electronic equipment and portable devices are also incorporating CB to make use of its outstanding electrical conductivity.[10-11]

Typically, RGO is obtained by partial chemical or thermal reduction of graphene oxide platelets (GO) prepared by a modified Hummers method.[12-14] In this way, the graphitic network structure can be restored in RGO exhibiting excellent electrical

conductivity, mechanical and optical properties. These benefits bring RGO a number of applications in electronics and energy storage.[15-20] Generally, as a sheet-like material, the aspect ratio for RGO is very high, in the order of 10^3-10^4. This led to a much lower percolation threshold for RGO that makes RGO very promising towards reducing carbon content applications such as conductive composites and battery electrodes.[21]

Given the exceptional characteristics of CB and RGO, investigating the rheological behavior and microstructure of their suspensions is also important for better understanding and handling in the manufacturing processes. In terms of imaging, cryogenic scanning electron microscopy (cryo-SEM) shows its excellence in preserving structures at frozen and nearly natural hydrated states, allowing us to examine the "real" morphology of studied specimens straightforwardly. The distortion of sample resulting from the drying process typically for conventional SEM can be avoided by this method.[22-24]

The objective of this study is to investigate the rheological properties and microstructures of aqueous suspensions of CB and mixtures of CB and RGO in a range of CB concentrations utilizing rheology experiments and cryo-SEM imaging. CB used in this work is a commercial product with surface functionalization. Previous research studies have demonstrated some unique properties of this CB such as excellent emulsifying capability and electrical conductivity, leading to potential use in oil spill remediation and lithium ion batteries.[25-28]

4.3 Materials and methods

A 15 wt% para-amino benzoic acid (PABA)-terminated carbon black (CB) in aqueous suspension at pH 7.5 was provided by Cabot Corporation. Every CB particle is composed of primary particles approximately 20 nm each in diameter, fused into a fractal aggregate of average nominal dimensions ~150 nm. At pH 7.5, the carboxyl groups on CB are deprotonated. This makes CB particles highly hydrophilic leading to a stable suspension in water. Reduced graphene oxide nanoplatelets (RGO) were purchased from Graphene Supermarket, with a specific surface area ~833 m^2/g and carbon/oxygen ratio 10.5. The average particle lateral size is ~4 μm. Hydrochloric acid (HCl, 37 wt%) was purchased from Sigma Aldrich. Deionized water was obtained from a Millipore Milli Q system.

A 1 mg/ml RGO suspension in water was prepared by probe sonication. Appropriate volumes of this RGO suspension and CB stock suspension were well mixed with deionized water by bath sonication. In the final aqueous mixtures, CB mass ratios were 0.05 -7.5wt%, and RGO concentrations were 0.01wt% and 0.05wt%. Identical concentrations of CB suspensions with no RGO served as control. 1M HCl was added to some of the suspensions to adjust pH to 3 or 5 while others remained the neutral pH ~7.5. Various pH values were chosen due to the pH dependence of CB, where the surface carboxyl groups on CB are responsive to pH change.[26] This in turn affects the structure and properties of the mixtures containing CB and RGO.

Cryogenic Scanning Electron Microscopy (cryo-SEM, Gatan Alto 2500 cryo preparation system attached to a Zeiss Sigma field emission scanning electron microscope) was used to look at the structure of prepared suspensions.

An AR2000ex rheometer with a cone and plate as the geometry was employed for running rheological measurements. All testing was conducted at 25°C. To determine the appropriate shear stress for viscosity testing to a range of shear rates, the samples were required to be within the linear viscoelastic region. Within this region, viscoelastic properties are independent of stress or strain levels, which was required for the accuracy of future testing. All samples were vortexed at 3000 rpm for 30 seconds, and testing began within 1 minute right after vortexing. The samples were pre-sheared at 0.1 s^{-1} for 60 seconds to remove any shearing history before doing the measurements. The samples were first tested for a change in dynamic viscosity with respect to a change of shear rate, in the range of 3-2000 s^{-1}. Upon completion, the samples were tested for the viscoelastic response. Storage and loss moduli were obtained with increasing angular frequency ranging from 0.01 to 10 rad/s.

4.4 Results and discussion

Figure 4.1 shows the rheology of CB particle suspensions at different pH conditions. Apparently, there was a strong dependence of viscosities on pH values. At pH 7.5, CB suspensions show Newtonian behavior at all concentrations between 0.05 wt% to 10 wt% (Figure 4.1A). As pH was reduced to 5, only 10wt% CB suspension showed shear thinning behavior and there was a monotonic decrease in viscosity with increased shear rate below 100 s^{-1}. At higher shear rates, the flow curves leveled off to a Newtonian plateau. All the other CB suspensions still exhibited Newtonian behavior (Figure 4.1B). With further pH decreased to 3, similar shear thinning behavior was observed in CB suspensions at concentrations of 1.5-10wt% (Figure 4.1C). As mentioned before, CB particles had surface carboxylate groups which deprotonated at

neutral pH causing a negative surface charge on CB. There was repulsive interaction between CB particles. Addition of the acid protonated some of these groups and increased the surface charge, the repulsion of CB particles was reduced. Some CB started to form aggregates which immobilized part of the matrix inside them and therefore increased the effective solids volume fraction in the suspension and its viscosity.[29] As shear thinning occurred in much lower concentrations of CB at pH 3, the degree of CB aggregation at pH 3 was much larger than pH 5.

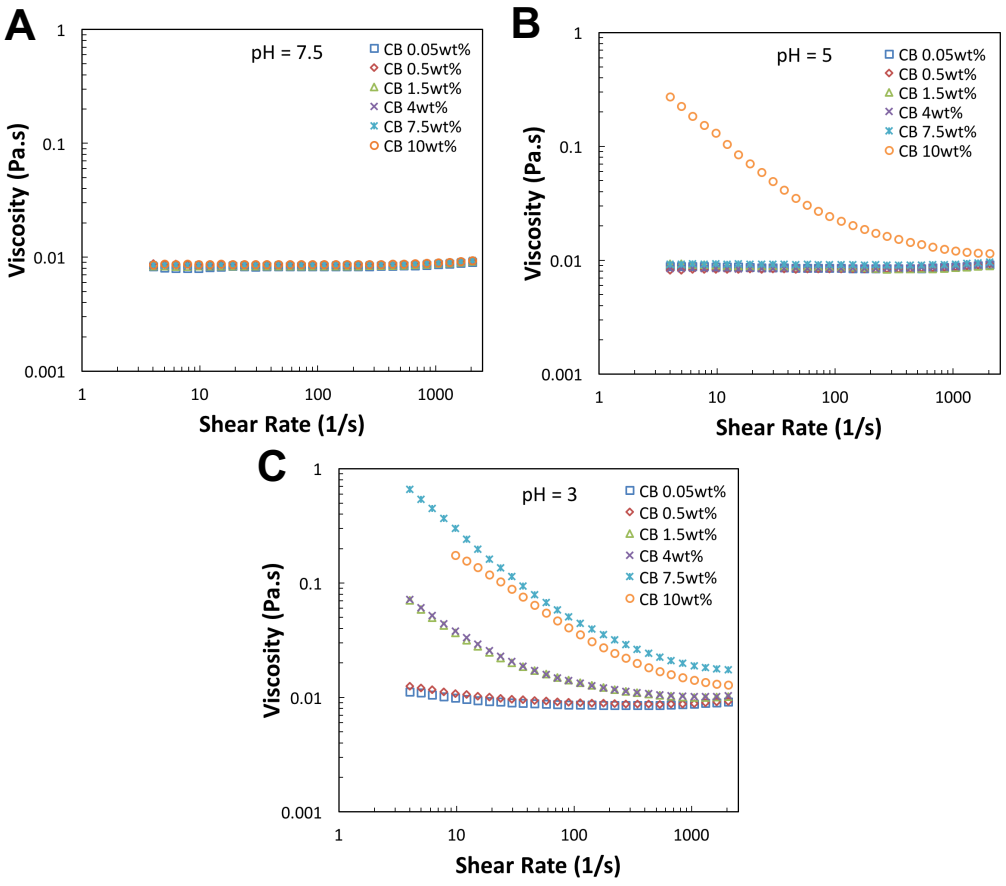

Figure 4.1. Plots of viscosity vs. shear rate for CB suspensions at different concentrations. (A) At pH 7.5, (B) At pH 5 and (C) At pH 3.

Towards reducing carbon content in the suspensions for future applications such as electrode slurries for lithium ion batteries, pH 3 was more effective with a lower CB concentration to form aggregation as well as network. Oscillatory frequency sweep experiments were performed at an oscillatory stress of 1Pa within the linear viscoelastic region to investigate the structures of the CB suspensions at 0.05-10wt% at pH 3. In Figure 4.2, we only present the valid data points where raw phase angle is below 175 degree and the system inertia is not dominant in this case. at 7.5% CB with frequency below 0.1 rad/s, a plateau region where G' equals to G" can be observed, indicating a gel formation in the sample which correlated with an elastic network structure. However, this structure broke down as the frequency increased showing splitting of G' and G". Afterwards, G" was always above G' in the tested frequency range, showing a viscous behavior. For G', it first slowly dropped with increasing frequency till 2 rad/s, then bounced back and gradually went up close to G" again. This possibly suggested a reorganization of the broken structure in the suspension. For the other samples in the range of 1.5-10wt% CB, all suspensions showed a more fluid-like behavior with G">G' at low frequencies. Their crossover frequencies could not be accessed under current testing conditions. But a potentially solid-like behavior with G'>G" after crossover at medium-high frequencies can be predicted from the trends of G' and G". The moduli curves for samples below 1.5wt% CB are not shown here as they pretty much overlapped with the one at 1.5wt%.

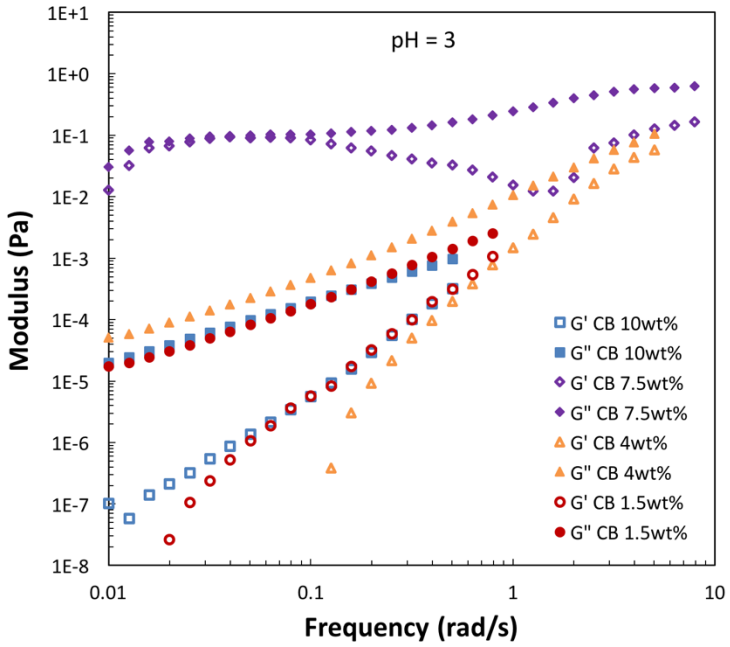

Figure 4.2. Elastic (G', open symbols) and viscous (G", solid symbols) moduli for CB suspensions at pH 3.

Figure 4.3 shows the evolution of microstructure in CB suspensions at pH 3 with increasing concentrations by cryo-SEM imaging. At concentrations below 1.5wt%, only a few discrete CB aggregates were randomly distributed in water due to the attraction among the partially hydrophobic CB particles (Figures 4.3A-B). These aggregates did not affect the viscosities of the suspensions. At 1.5wt% CB, some parts of CB aggregates were connected (Figure 4.3C). As the concentration increased to 4wt%, a partially connected network was formed by CB particles (Figure 4.3D). The partial network formation caused a increase of the viscosities for the suspensions at these two CB concentrations. When CB reached 7.5wt% in suspension, a transient network was observed with a slightly shear-induced orientation indicating a weak gel fromation (Figure 4.3E). This was consistent with the flow and osillatory results showing high viscosity and high moduli. The shear possibly resulted from the cryo sample preparation. A transient network with no obvious orientation was formed with

large areal aggregates at 10 wt% CB, which agreed with the reduced viscosity and decreased moduli restults (Figure 4.3F). For CB at or above 7.5wt%, the dramatically increased viscosities of the suspensions were attributed to the transient network formation.

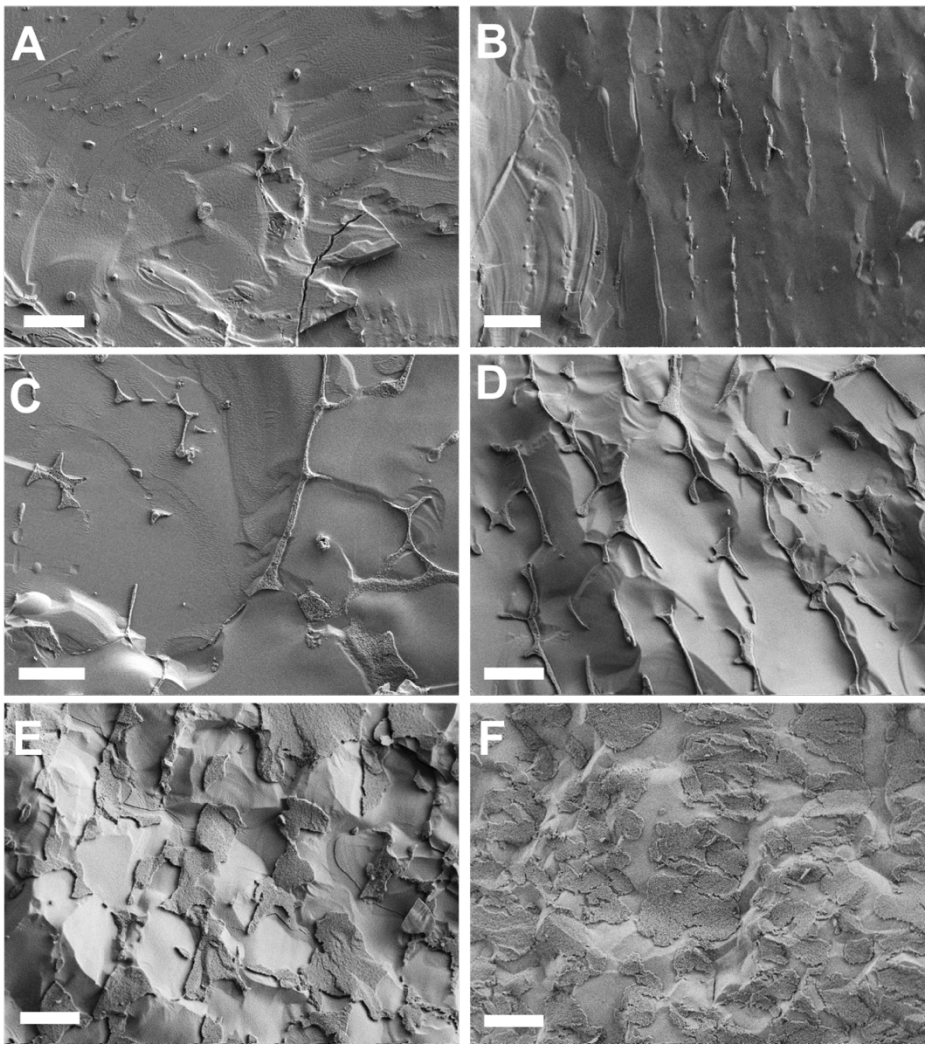

Figure 4.3. Cryo-SEM images of CB suspensions at pH 3 at different concentrations. (A) 0.05wt% CB, (B) 0.5wt% CB. In (A) and (B), only few aggregates consisting of CB particles were observed. (C) 1.5wt% CB, some connections can be seen in the CB aggregates. (D) 4wt% CB, a partially connected network was formed by CB particles. (E) 7.5wt% CB, a transient network was seen with a shear-induced orientation. (F) 10wt% CB, a transient network with no obvious orientation was formed with large areal aggregates. Scale Bars = 10μm.

At CB concentrations below 7.5wt% where no network was observed, we examined if addition of RGO influenced the rheological behavior and microstructure of the mixed suspensions at pH 3. As 4wt% CB, as shown in Figure 4.4, the viscosities of the mixed suspensions with RGO at both mass ratios 0.01wt% and 0.05wt% were nearly identical to that with no RGO (Figure 4.4A). Storage and loss moduli remained the same values and trend for all of the three samples (Figure 4.4B). Cryo-SEM imaging showed that RGO was mostly embedded in the CB aggregates in both suspensions (Figure 4.4C). This was due to the attraction between CB and RGO with certain hydrophobicity at acidic condition. As CB concentration was much higher than that of RGO, addition of RGO was not sufficient to change the microstructures. Therefore, RGO addition was not helpful in forming network at medium CB concentrations.

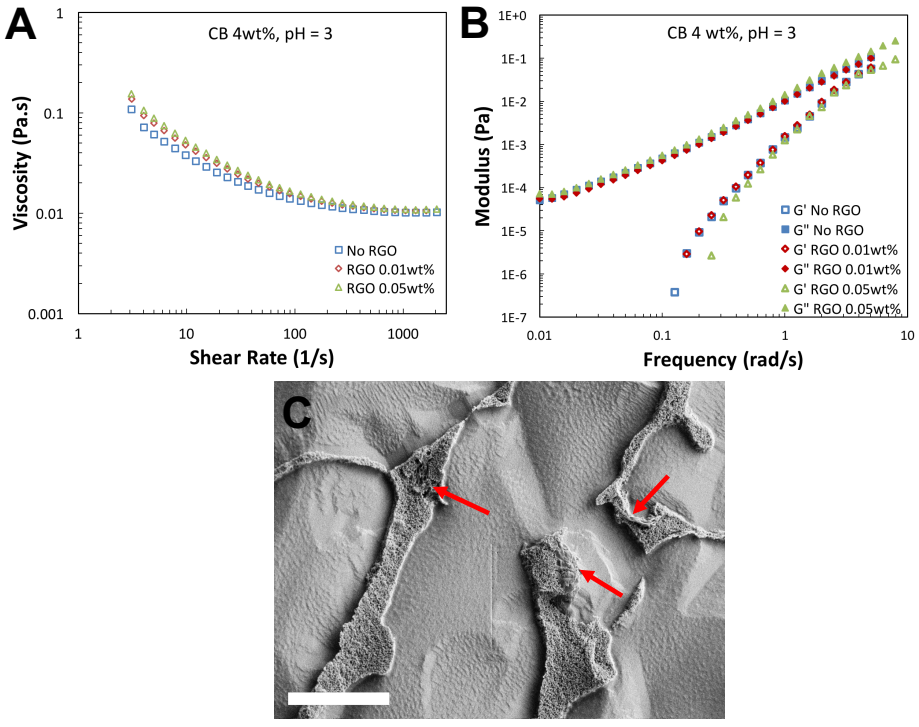

Figure 4.4. Plot of viscosity vs. shear rate (A), storage and loss moduli (B) for CB suspensions with and without RGO at 4wt% CB at pH 3. (C) A cryo-SEM image for sample (4wt% CB+0.05wt% RGO). RGO sheets marked by red arrows were embedded in CB aggregates. Scale Bar = 5μm.

With CB concentration further decreasing, at 1.5wt% and 0.5wt% CB, 0.01wt% RGO addition did not cause a change in the viscosity of mixture suspension, while there was an order of magnitude increase in viscosity when 0.05wt% RGO was introduced (Figures 4.5A and B). However, for both samples, the storage and loss moduli with added RGO did not cause any change, indicating only slight or no structural transorfomation (Figures 4.5C and D). Cryo-SEM images (Figures 4.5E and F) showed at low CB concentrations, with 0.05wt% RGO, RGO was dominant in forming the connections with some CB particles binding on RGO and it was beneficial for the partial network formation as backbones. This led to a viscosity increase in the mixed suspensions. But this effect was negligible in terms of the whole sample structure. For 0.05wt% CB, due to the total low concentration of CB and RGO, the mixture suspensions with lower or higher RGO concentrations showed the same viscosities as the one with no RGO with a Newtonian behavior, and there was no change in moduli as well. Therefore, the results were not shown in this work.

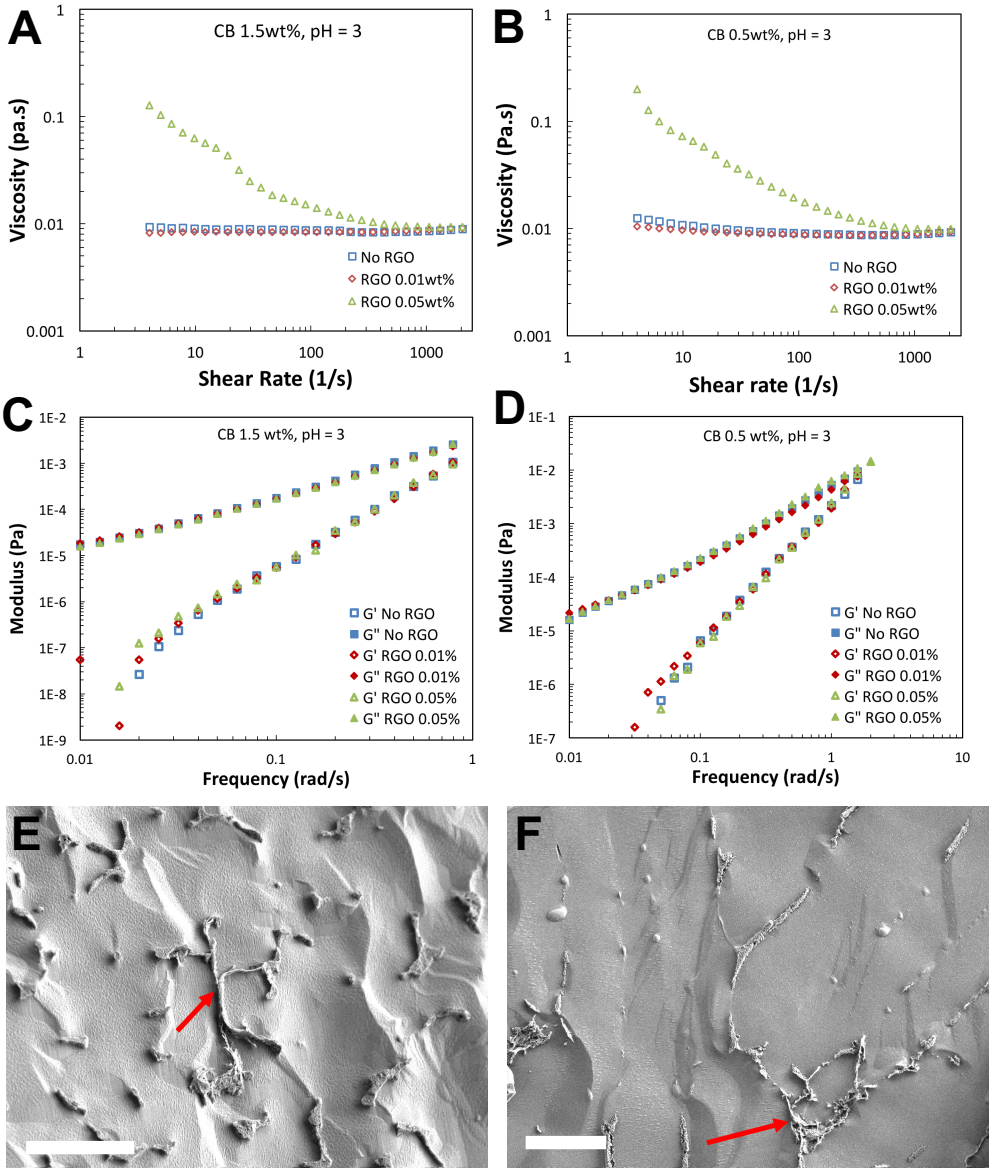

Figure 4.5. Plots of viscosity vs. shear rate (A, B), storage and loss moduli as a function of frequency (C, D) and cyro-SEM images (E, F) for CB suspensions with and without RGO at pH 3. (A, C) 1.5wt% CB, (B, D) 0.5wt%CB, (E) 1.5wt% CB+0.05wt% RGO (F) 0.5wt% CB+0.05wt% RGO. In E and F, RGO sheets marked by red arrows were dominant in forming some connections with CB particles binding on RGO. Scale Bars = 10μm.

4.5 Conclusions

We studied the rheological behavior and microstructures of the suspensions of CB and the mixture of CB and RGO in water. It turned out that pH value and CB

concentration both had significant effects on the viscosities and microstructures of CB suspensions. An obvious viscosity increase showing shear thinning behavior for CB above 0.5wt% was observed at pH 3 compared to pH 5 and 7.5. Cryo-SEM images showed the microstructure evolution of CB suspensions from forming aggregates to transient network at pH 3. Addition of high wt% RGO in suspensions containing 0.5wt% and 1.5wt% CB at pH 3 led to a viscosity increase corresponding to a microstructure change with RGO as the dominant component for forming connections. However, the storage and loss moduli with added RGO did not show much difference from the one with no RGO, indicating no significant structural transition in the whole sample.

4.6 Acknowledgements

We gratefully acknowledge funding from Department of Energy, Office of Basic Energy Sciences, EPSCoR Implementation award DE-SC0007074.

4.7 References

1. Darmstadt, H.; Roy, C.; Kaliaguine, S., Characterization of pyrolytic carbon blacks from commercial tire pyrolysis plants. *Carbon* **1995,** *33* (10), 1449-1455.

2. Studebaker, M. L., The chemistry of carbon black and reinforcement. *Rubber Chemistry and Technology* **1957,** *30* (5), 1400-1483.

3. Medalia, A., Effect of carbon black on dynamic properties of rubber vulcanizates. *Rubber chemistry and Technology* **1978,** *51* (3), 437-523.

4. Mansour, K.; Soileau, M.; Van Stryland, E. W., Nonlinear optical properties of carbon-black suspensions (ink). *JOSA B* **1992,** *9* (7), 1100-1109.

5. Spinelli, H. J., Polymeric dispersants in ink jet technology. *Advanced Materials* **1998,** *10* (15), 1215-1218.

6. Medalia, A.; Richards, L., Tinting strength of carbon black. *Journal of Colloid and Interface Science* **1972,** *40* (2), 233-252.

7. Huang, J. C., Carbon black filled conducting polymers and polymer blends. *Advances in Polymer Technology* **2002,** *21* (4), 299-313.

8. Balberg, I., A comprehensive picture of the electrical phenomena in carbon black–polymer composites. *Carbon* **2002,** *40* (2), 139-143.

9. Sumita, M.; Sakata, K.; Asai, S.; Miyasaka, K.; Nakagawa, H., Dispersion of fillers and the electrical conductivity of polymer blends filled with carbon black. *Polymer Bulletin* **1991,** *25* (2), 265-271.

10. Lonergan, M. C.; Severin, E. J.; Doleman, B. J.; Beaber, S. A.; Grubbs, R. H.; Lewis, N. S., Array-based vapor sensing using chemically sensitive, carbon black−polymer resistors. *Chemistry of Materials* **1996,** *8* (9), 2298-2312.

11. Ryan, M.; Shevade, A.; Zhou, H.; Homer, M., Polymer–carbon black composite sensors in an electronic nose for air-quality monitoring. *MRS bulletin* **2004,** *29* (10), 714-719.

12. Pei, S.; Cheng, H.-M., The reduction of graphene oxide. *Carbon* **2012,** *50* (9), 3210-3228.

13. Stankovich, S.; Dikin, D. A.; Piner, R. D.; Kohlhaas, K. A.; Kleinhammes, A.; Jia, Y.; Wu, Y.; Nguyen, S. T.; Ruoff, R. S., Synthesis of graphene-based nanosheets via chemical reduction of exfoliated graphite oxide. *carbon* **2007,** *45* (7), 1558-1565.

14. Zhu, Y.; Murali, S.; Cai, W.; Li, X.; Suk, J. W.; Potts, J. R.; Ruoff, R. S., Graphene and graphene oxide: synthesis, properties, and applications. *Advanced materials* **2010,** *22* (35), 3906-3924.

15. Eda, G.; Fanchini, G.; Chhowalla, M., Large-area ultrathin films of reduced graphene oxide as a transparent and flexible electronic material. *Nature nanotechnology* **2008,** *3* (5), 270-274.

16. He, Q.; Wu, S.; Yin, Z.; Zhang, H., Graphene-based electronic sensors. *Chemical Science* **2012,** *3* (6), 1764-1772.

17. Wang, D.; Choi, D.; Li, J.; Yang, Z.; Nie, Z.; Kou, R.; Hu, D.; Wang, C.; Saraf, L. V.; Zhang, J., Self-assembled TiO2–graphene hybrid nanostructures for enhanced Li-ion insertion. *ACS nano* **2009,** *3* (4), 907-914.

18. Zhang, Q.; Li, R.; Zhang, M.; Zhang, B.; Gou, X., SnS 2/reduced graphene oxide nanocomposites with superior lithium storage performance. *Electrochimica Acta* **2014,** *115*, 425-433.

19. Zhang, W.; Zhang, Y.; Tian, Y.; Yang, Z.; Xiao, Q.; Guo, X.; Jing, L.; Zhao, Y.; Yan, Y.; Feng, J., Insight into the capacitive properties of reduced graphene oxide. *ACS applied materials & interfaces* **2014,** *6* (4), 2248-2254.

20. Zhu, X.; Zhu, Y.; Murali, S.; Stoller, M. D.; Ruoff, R. S., Nanostructured reduced graphene oxide/Fe2O3 composite as a high-performance anode material for lithium ion batteries. *Acs Nano* **2011,** *5* (4), 3333-3338.

21. Zhang, Y.; Pan, Y.; Chen, Y.; Lucht, B. L.; Bose, A., Towards reducing carbon content in silicon/carbon anodes for lithium ion batteries. *Carbon* **2017,** *112*, 72-78.

22. Hassan, A.; Frank, J.; Elsoda, M., Observation of bacterial exopolysaccharide in dairy products using cryo-scanning electron microscopy. *International Dairy Journal* **2003,** *13* (9), 755-762.

23. Issman, L.; Talmon, Y., Cryo-SEM specimen preparation under controlled temperature and concentration conditions. *Journal of microscopy* **2012,** *246* (1), 60-69.

24. Milne, J. L.; Borgnia, M. J.; Bartesaghi, A.; Tran, E. E.; Earl, L. A.; Schauder, D. M.; Lengyel, J.; Pierson, J.; Patwardhan, A.; Subramaniam, S., Cryo-electron microscopy–a primer for the non-microscopist. *The FEBS journal* **2013,** *280* (1), 28-45.

25. Chen, Y.; Xu, M.; Zhang, Y.; Pan, Y.; Lucht, B. L.; Bose, A., All-Aqueous Directed Assembly Strategy for Forming High-Capacity, Stable Silicon/Carbon Anodes for Lithium-Ion Batteries. *ACS applied materials & interfaces* **2015,** *7* (38), 21391-21397.

26. Saha, A.; Nikova, A.; Venkataraman, P.; John, V. T.; Bose, A., Oil emulsification using surface-tunable carbon black particles. *ACS applied materials & interfaces* **2013,** *5* (8), 3094-3100.

27. Godfrin, M. P.; Tiwari, A.; Bose, A.; Tripathi, A., Phase and steady shear behavior of dilute carbon black suspensions and carbon black stabilized emulsions. *Langmuir* **2014,** *30* (51), 15400-15407.

28. Katepalli, H.; John, V. T.; Bose, A., The response of carbon black stabilized oil-in-water emulsions to the addition of surfactant solutions. *Langmuir* **2013,** *29* (23), 6790-6797.

29. Barthelmes, G.; Pratsinis, S.; Buggisch, H., Particle size distributions and viscosity of suspensions undergoing shear-induced coagulation and fragmentation. *Chemical Engineering Science* **2003,** *58* (13), 2893-2902.